Spectral Changes during the 0.1-4 Hz Quasi-Periodic Oscillations in the Black Hole X-ray Binary XTE J1550-564

by

Steven N. Cho

B.S., Physics, United States Military Academy (1995)

Submitted to the Department of Physics
in partial fulfillment of the requirements for the degree of

Master of Science

at the

MASSACHUSETTS INSTITUTE OF TECHNOLOGY

June 2005

Author . . . .
Department of Physics
May 6, 2005

Certified by. . . . .
Walter H. G. Lewin
Professor of Physics
Thesis Supervisor

Accepted by . . . .
Thomas Greytak
Professor of Physics
Associate Department Head for Education
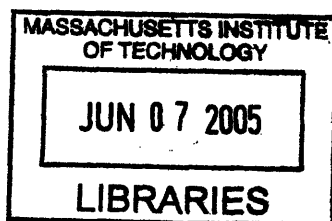
Spectral Changes during the 0.1-4 Hz Quasi-Periodic Oscillations in the Black Hole X-ray Binary XTE J1550−564

by

Steven N. Cho

Submitted to the Department of Physics
on May 6, 2005, in partial fulfillment of the
requirements for the degree of
Master of Science

Abstract

In this thesis, we describe the analysis of 0.1-4 Hz quasi-periodic oscillations (QPOs) of the black hole X-ray binary XTE J1550−564 using data obtained with the *Rossi X-ray Timing Explorer (RXTE)* satellite. Data from 13 consecutive observations spanning eight days were included in this analysis. By comparing the spectra of the source when it is in the *high* intensity phase with the *low* intensity phase of its QPO cycle, we hoped to gain insight into the cause of QPOs and how they relate to structures and processes in the vicinity of black holes. Like observations from the black hole X-ray binary GRS 1915+105 (Miller and Homan 2005), our observations from XTE J1550−564 showed a significant difference in the Fe Kα line equivalent width between the *high* and *low* intensities of the QPO for 6 of 13 observations. However, 2 of 13 observations exhibited the opposite effect in that the Fe Kα line equivalent width actually dropped significantly during periods of *high* intensity. Moreover, we found that the integrated flux of the Fe Kα line was proportional to the flux of the continuum in 5 of 13 observations. Despite these competing effects, the ratios of the *low* intensity and *high* intensity spectra indicate an increase in the QPO strength up to about 10 keV, above which it decreases only slightly. We also found dramatic changes in the QPO strength at low energies as the QPO frequency increases. We believe this to be the result of an increase in relative contributions to the spectra as the disk blackbody component becomes more important. In this thesis, we discuss five possible spectral models to explain QPOs based on the behavior of Fe Kα emission lines. Then we describe whether or not our results agree with those predictions. Although our results show correlations similar to those found by Miller and Homan (2005), they also show anti-correlations in several observations. Our results support Miller and Homan's suggestion of a link between discrete timing features (QPOs) and spectral features (Fe Kα emission lines) which occur in the inner disk around black holes. Our work shows that current explanations for QPOs have some physical basis, suggesting that QPOs are due to either a quasi-periodically changing reflector area in the accretion disk or an episodic modulation of the hard flux component in the corona or jets that irradiates the accretion disk. Our results also suggest that perhaps the correct model is something more complex that goes beyond current models and is able to explain the multiple effects observed in the Fe Kα line.

Thesis Supervisor: Walter H. G. Lewin
Title: Professor of Physics

Acknowledgments

Contents

List of Figures

List of Tables

Chapter 1

Introduction

When we look at black hole candidates, we see different types of variability in the intensity of emitted radiation. An interesting type of variability occurs when the source intensity changes in an almost periodic fashion; we call such variability "quasi-periodic oscillations" (QPOs). No single theory uniquely describes all of the observed quasi-periodic oscillations (QPOs) in black holes. The black hole X-ray binary XTE J1550−564 is of particular interest because it displays a variety of QPOs, which can be used to investigate the accretion process around black holes. Previous studies have shown a strong correlation between the temporal characteristics of black holes and their spectral state. QPOs are fundamental properties of the accretion flow, and in a few sources like XTE J1550−564, the rms amplitude of the QPOs can exceed ∼15% of the mean X-ray flux. Simultaneous studies of both the temporal and spectral properties of black holes show promise of determining the origin of QPOs in these sources.

The focus of our work is to investigate the connection between the temporal and spectral properties of XTE J1550−564. Whereas most studies consider either the temporal or the spectral properties of X-ray emission, our work combines both simultaneously. By comparing the spectra of the source when it is in the *high* intensity phase with the *low* intensity phase of its QPO cycle, we hope to gain insight into the cause of QPOs and how they relate to structures and processes in the vicinity of black holes. The large collecting area (∼6250 cm^2) of the *Rossi X-ray Timing Explorer (RXTE)* facilitates the detection of many photons in short time periods, which is essential for the study of rapidly varying X-ray QPOs. Furthermore, the microsecond timing resolution of *RXTE* is more than sufficient to detect and analyze QPOs with frequencies in the 0.1-4 Hz range. Thus, we have the source and means to obtain greater insight into processes that occur on characteristic time scales near black holes.

We begin in Chapter 1 by presenting a review of the source, the instrument used to study it, and the mechanisms at work. In Chapter 2, we describe our methods and techniques used to analyze the data. Chapter 3 contains the results of our work. In Chapter 4, we discuss the impact our results have on current and future models. Chapter 5 closes with the conclusions from our work.

1.1 X-ray Binaries

A detailed understanding of the structure and evolution of stars requires knowledge about their physical characteristics, such as mass, radius, luminosity, effective temperature, and

composition. Because most stars are so far away, it is difficult to determine their properties directly by using even our most powerful telescopes. Fortunately, nature has provided ample opportunity for astronomers to observe what is known as binary star systems. At least half of all "stars" in the Milky Way are actually multiple systems consisting of two or more stars in orbit around a common center of mass.

A wealth of information is available from a binary system even if it is not possible to resolve each of its stars individually. In many cases, important stellar characteristics can be determined from the interaction of stars in the system. Such characteristics include the stars' individual masses and radii as well as the ratio of their fluxes (and, hence, the ratio of their effective temperatures). These results are important because they can then be used to develop theories of stellar structure and evolution.[1]

In this thesis, we focus on a special type of binary in which one of the stars is a compact object. In these so-called X-ray binaries, a compact object (a neutron star or a stellar mass black hole) is accreting matter from a companion star. Mass transfer in these systems gives rise to processes that emit in the X-ray band of the electromagnetic spectrum. As matter flows from the donor to the accretor, angular momentum prevents it from being captured directly by the compact object. As a result, an accretion disk is formed around the compact object (see Figure 1-1).
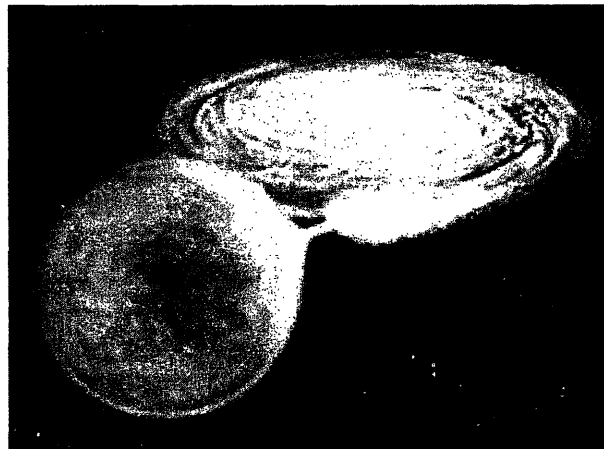
Figure 1-1: Accretion disk, formed when a compact object captures matter from a companion star. (Picture courtesy of NASA.)

The mechanism for mass transfer into the disk takes two forms: strong stellar winds and Roche lobe overflow. Massive, luminous donor stars drive matter away from their surfaces in the form of strong stellar winds (see Figure 1-2). As these strong winds carry matter away from the donor, they become susceptible to the strong gravitational attraction of the accretor, thus forming an accretion disk. Smaller, less massive stars, on the other hand, achieve mass transfer by overflowing their Roche lobes. When the atmosphere of the donor star expands to what is known as the "inner Lagrangian point" (see Figure 1-3) between the two stars, the matter reaches an equipotential at which point matter is attracted equally to both stars (see Figure 1-2). As a result, some mass flows through the inner Lagrangian point and toward the compact object, forming an accretion disk. In both cases, internal friction and tidal effects transfer and remove angular momentum through and from the disk, allowing the matter to eventually fall onto the compact object.

---

[1]For a more detailed review of binary stars, see Bate (2004).
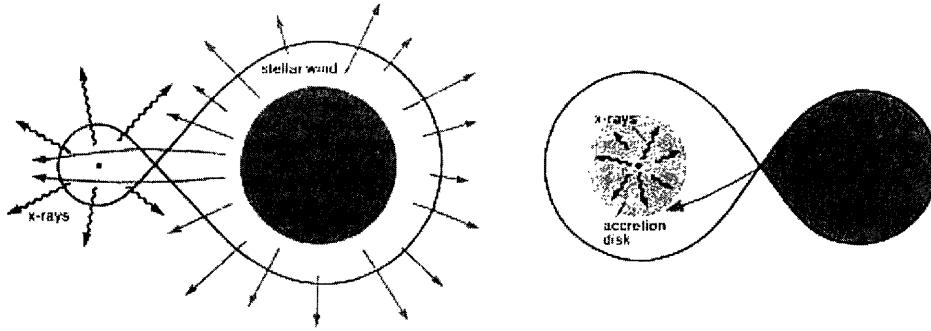
Figure 1-2: Mass transfer, showing stellar winds in an HMXB (left) vs. Roche lobe overflow in an LMXB (right) (Taam and Fryxell 1989).
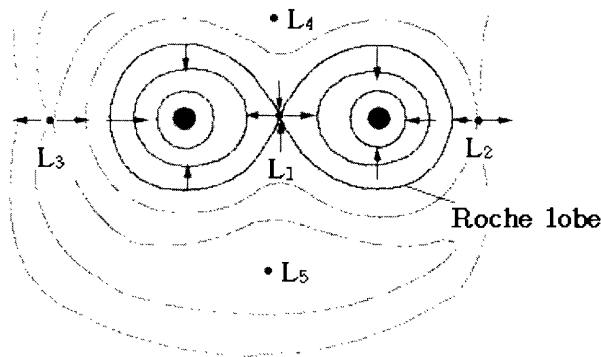
Figure 1-3: Lines of equipotential around two stars; a star fills its Roche lobe when it expands to L1, the inner Lagrangian point.

Through analysis of their optical spectra, binary star systems that emit in the X-ray can be classified as either high-mass X-ray binaries (HMXBs) or low-mass X-ray binaries (LMXBs). As the names imply, differences between the two classifications are rooted in the masses of the stars. The masses of the stars and their orbital separation determine whether or not the donor star will fill its Roche lobe. If the compact object is much more massive than the donor star, then the inner Lagrangian point will be located close to the donor star, allowing the donor star to overflow its Roche lobe more easily. On the other hand, if the donor star is more massive, then the inner Lagrangian point will be located further from the donor, making Roche lobe overflow more difficult to achieve. However, massive stars have strong stellar winds that can create an accretion disk in lieu of Roche lobe overflow. Through observations of its optical properties, a binary system's donor mass can be determined and, hence, its binary classification (LMXB or HMXB) can be made.

In general, optical counterparts of HMXBs have the appearance of normal early-type stars, making their spectra easy to classify. Because the bolometric luminosity of the mass donor generally exceeds the X-ray luminosity of the central X-ray source, the appearance of an HMXB is largely unaffected by the X-ray source. In other words, the intrinsic luminosity of the donor star is much greater than the induced luminosity from X-ray heating by the compact object. Because the mass donor is a giant or supergiant with high mass ($> 10 M_\odot$), mass transfer may be achieved through either Roche lobe overflow or through strong stellar winds. Most HMXBs are X-ray pulsars, indicating the presence of a neutron star.

17

The optical spectrum of an LMXB makes its appearance unlike any ordinary star. In an LMXB, X-ray heating of the accretion disk and the companion star dominates the optical emission, so the spectrum looks like emission lines superposed on a blue continuum. The disk absorbs a large fraction of the X-rays from the central source and reprocesses them into optical and UV photons. The optical contribution from the donor star is very small. Moreover, the low mass of the evolved donor ($< 10 M_\odot$) makes stellar winds negligible, so mass transfer must be achieved through Roche lobe overflow.[2]

1.2 X-ray Emission

Regardless of the accretion mechanism, X-rays are emitted by very energetic processes in the vicinity of compact objects and in hot ionized gases (plasmas). Photons in the X-ray band have energies of $\sim$0.1-100 keV, which, for thermal radiation, corresponds to temperatures of $\sim$1 million-1 billion K. As in other wavebands, both line and continuum emission are observed simultaneously. The study of X-ray emission becomes paramount in cases where a celestial body cannot be studied in other wavebands.

X-ray emission from astronomical sources is attributed to three dominant physical processes: thermal bremsstrahlung, synchrotron radiation, and blackbody radiation. Each process gives a unique spectral signature, thereby revealing clues about the nature of the X-ray source. If the spectrum can be measured with a high resolution over a broad energy band, then both the emission process as well as the physical conditions of the source can usually be determined.

1.2.1 Thermal Bremsstrahlung Radiation

At temperatures above 10^5 K, atoms are ionized, and a gas consists of positive ions and negative electrons. The thermal energy of the gas is shared among the particles and is transferred rapidly between the particles through collisions. In "thermal equilibrium," the average energy of the particles is the same, and that energy is determined by the temperature of the gas. When an electron passes close to a positive ion, its trajectory changes in response to the strong electric forces. The acceleration of the electron from this interaction causes the release of electromagnetic radiation known as "bremsstrahlung," or "braking radiation."

Electrons in thermal equilibrium have a well-defined distribution of velocities. Hence, the radiation from electron-ion collisions results in a continuum with a characteristic shape that is determined only by temperature. This is known as "thermal bremsstrahlung." The thermal bremsstrahlung spectrum falls off exponentially at high energies and is characterized by the temperature. Higher temperatures mean faster electrons, which, in turn, produce higher-energy photons. When the temperature rises above $\sim$1 million K, the photons are predominantly X-rays.

1.2.2 Synchrotron Radiation

When a fast-moving electron passes through a strong magnetic field, its trajectory changes in response to the Lorentz force perpendicular to the direction of motion. Because the electron is accelerated, it releases electromagnetic energy called "synchrotron" radiation. The frequency of the radiation depends only upon the electron energy, the magnetic field strength, and the direction of motion relative to the field.

---

[2]For a more detailed review of X-ray binaries, see van Paradijs and McClintock (1995).

However, in an astrophysical setting, the magnetic field can be somewhat aligned with the axis of rotation of the compact object, but particle velocities are expected to be isotropic. Therefore, the observed spectrum depends only upon the magnetic field strength and the electron energy spectrum. The spectrum resulting from synchrotron radiation takes the form of what is known as a power law. Power laws are important because they describe the energy dependence of the continuum emission near compact objects. A larger value of the power law index means a softer spectrum.

1.2.3   Blackbody Radiation

The third process for X-ray emission is through blackbody radiation. A "blackbody" has a surface that completely absorbs all radiation incident upon it. Reflectivity is zero. However, the surface must emit radiation, and the radiated spectrum is a well-defined continuum whose peak emission occurs at an energy specified by the temperature. Higher temperatures mean more energetic photons, so the emission peaks at higher energies. Stars radiate as blackbodies with temperatures from 2500 K (red dwarf) to 40,000 K (O star). Although the stellar atmosphere strongly modifies a star's spectrum, spectra formed by the blackbody emission process retain their overall gross shape. If a hot surface reaches a temperature of 1 million K or higher, it will emit blackbody radiation in the X-ray band. This fact is important because accretion disks around compact objects can reach these high temperatures, and proof of the blackbody emission process can be found in the spectra.

1.2.4   Comptonization

Interactions between photons and electrons can also occur in what is known as "Comptonization." When a photon interacts with a free electron, it can transfer part of its energy to that electron. As a result, the electron gains energy while the photon loses energy. However, the opposite process, called " inverse Comptonization," can also occur. For example, if photons pass through a hot, ionized gas full of highly-energetic electrons, it is possible for the electrons to "upscatter" the photons to higher energies. This process is important in the study of how X-rays passing through a hot corona or relativistic jets from a compact object could get a boost in energy resulting from collisions with energetic electrons found in the gas. This could cause a hardening of the observed spectra as X-rays are boosted to higher energies.

1.2.5   Line Emission

In addition to the continuum, X-ray line emission can also be an important source of radiation in a hot gas. At high temperatures, atoms lose many of their electrons so that they are almost completely ionized. When a fast electron collides with an ion that has bound electrons, it can transfer energy to that ion, causing a transition to a higher energy level. The ion decays to its ground state by radiating photons of energy corresponding to the energy levels of the transitions. The result is a large number of possible energy transitions leading to line emission. Highly-ionized atoms produce transitions that release large amounts of energy, leading to an abundance of emission lines. Not only can the emission lines be used to determine the temperature of the gas, but relative strengths of the emission lines can also be used to determine relative abundances of the elements emitting them, thereby determining the chemical composition of the plasma from which the X-ray radiation emanates. An important X-ray emission line, called the Fe $K\alpha$ line, is observed

around 6.4 keV. It arises from an energy transition of electrons in iron atoms that have lost up to 26 electrons (a neutral iron atom has 26 electrons). As we will show, the Fe Kα line plays an important role in our research.

Fe Kα line emission occurs through a process called "fluorescence." Energetic X-rays irradiate the accretion disk, which contains iron. The high-energy photons free remaining electrons from the iron atoms. When the electrons return to their bound state, they release photons with a discrete amount of energy corresponding to the energy transition level. These emitted photons have less energy than the original absorbed photons because part of the energy is dissipated as vibrational and rotational energy of the electron. These photons appear in the spectra as Fe Kα emission lines.

1.2.6 Absorption

X-ray emission from the vicinity of the compact object propagates to the observer through the surrounding environment, which modifies the spectrum by absorption and scattering. Important zones of propagation include the accretion disk, the accretion disk corona/wind/jets, the wind and/or the atmosphere of the companion star, and, finally, the interstellar medium. As a result of these zones, the X-ray spectrum undergoes substantial absorption, particularly at low energies where an increased absorption cross-section occurs in the medium-Z elements such as iron, oxygen, and carbon. The observed spectra therefore contain absorption edges as well as emission lines from fluorescence and recombination. The relative edge to line strength gives clues to the geometry of the surrounding material. The line and edge energies can be used to constrain the ionization state of the material, which gives insight into its density and location.[3]

1.3 *RXTE*

All of the data used in our analyses were collected with the *Rossi X-ray Timing Explorer (RXTE)* (Bradt et al. 1993). *RXTE* was launched on December 30, 1995, and is still operational at the time of this writing. It was put into a low-earth circular orbit with an altitude of 580 km, an inclination of 23°, and a period of about 90 minutes. Due to its low orbit, *RXTE* has limitations in its ability to observe sources for extended periods of time. First, sources of interest can be occulted by the earth for as much as half of each orbit. Second, up to six times a day, *RXTE* passes through high particle flux areas of the South Atlantic Anomaly (SAA). This results in periods of 10-20 minutes for each passage during which some of the instruments are switched off. Thus, periods of uninterrupted data collection are usually limited to 1-2 ks.

RXTE was launched with the purpose of providing high time resolution with moderate spectral resolution for the study of variability in the emission of X-ray sources. The satellite consists of three primary scientific instruments: the Proportional Counter Array (PCA), the High-Energy X-ray Timing Experiment (HEXTE), and the All-Sky Monitor (ASM) (see Figure 1-4). Both the PCA and HEXTE are pointed instruments with co-aligned fields of view ($\sim 1°$) while the ASM is an independent scanning device that observes around 80% of the sky per orbit.

The PCA (see Figure 1-5) consists of five identical xenon-filled proportional counter units (PCUs) with a total collecting area of $\sim$6250 cm^2 (see Figure 1-6). Each PCU consists of

---

[3]For a more detailed review of X-ray emission, see White et al. (1995).
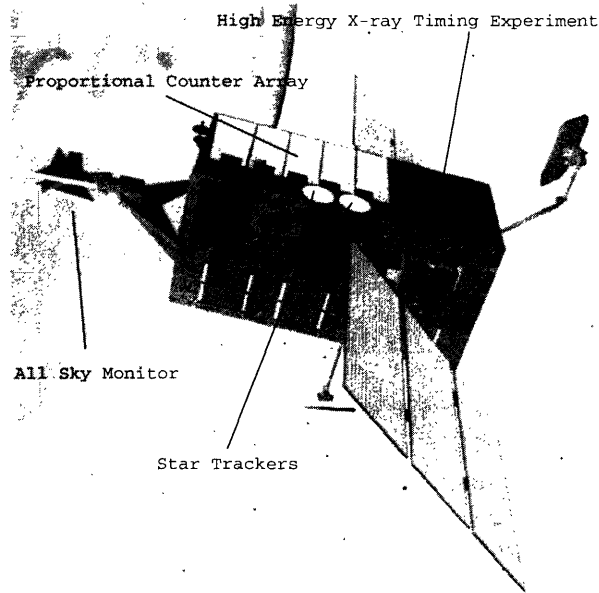
Figure 1-4: *RXTE*, showing the PCA, HEXTE, and ASM. (Diagram courtesy of NASA.)

five layers: one propane veto layer, three xenon signal layers (each split into two), and one xenon veto layer. Each PCU has sensitivity in the range 2-60 keV, spectral resolution of 18% at 6 keV, 255-channel pulse-height discrimination, and maximum time resolution of ~ 1 μs.

Three important strengths of *RXTE* are its large collecting area, its maneuverability, and its flexibility in changing data mode configurations. Its large collecting area (~ 6250 cm^2) enables the detection of many photons in a short time period, which is critical for the study of rapid QPOs. Moreover, its fast slew speed ($6°$ per minute) and its almost continuously available data link allow for follow-up observations within a few hours. Furthermore, *RXTE*
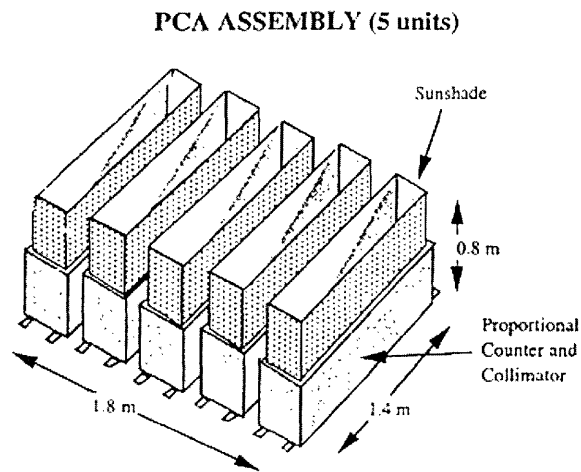
Figure 1-5: Proportional counter array (PCA) assembly, showing the five identical xenon-filled proportional counter units (PCUs). (Diagram courtesy of NASA.)

21

PROPORTIONAL COUNTER (1 unit)

Collimator
(hexagonal)
1° FWHM

X-ray
Shielding

Mylar
Windows
(25 μm)

Antico Layer
(Propane)

3.6 cm

3 Signal Layers
(Xenon/Methane)

Antico Chambers
(Xenon/Methane)

Anodes

Alpha
Detector

Americium Source

32.5 cm
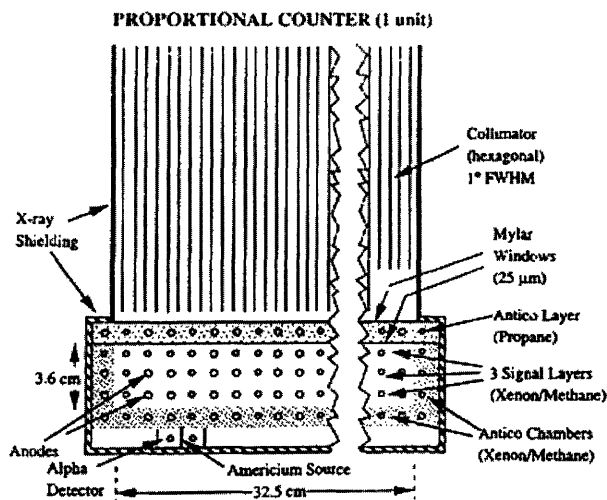
Figure 1-6: One of five proportional counter units (PCUs), showing the its multiple layers. (Diagram courtesy of NASA.)

enables observers to decide how the data will be processed. Its main on-board computers allow a large variety of data processing modes, which is especially important for bright sources. Hence, guest observers can decide whether to focus on spectral aspects, variability aspects, or a combination of both.

1.4   QPOs and Variability

The subject of this thesis is quasi-periodic variability with timescales of ~0.25-10 s in the X-ray emission of the X-ray binary XTE J1550−564. Professor Michiel van der Klis says the following about QPOs:

> The variations we are talking about are neither periodic, such as pulsations, dips, or eclipses; nor do they consist of easily recognized isolated events, such as X-ray bursts. They include the types of variability that are usually called quasi-periodic oscillations (QPOs) and noise, and also sometimes flickering, irregular flaring, fluctuations, etc. Such variability occurs in all types of X-ray binaries: black hole candidates, low-magnetic-field neutron star systems, and accreting pulsars.
>
> Together with X-ray spectroscopy, the study of rapid (periodic and aperiodic) X-ray variability is one of the very few ways to obtain direct information about the physical circumstances in the vicinity of accreting compact objects. The rapid aperiodic variability is thought to originate in the irregular nature of the inner accretion flow. As the flow is in close physical interaction with the compact object, some of the properties of the variability can be expected to reflect properties of the compact object. This is the main reason to study rapid aperiodic variability. Some of the information on the compact object can be extracted without a full understanding of the cause of the variability, such as, for example, turbulent and magnetic phenomena in the accretion disk.
>
> A well-defined resolved peak in the power spectrum is evidence for the presence

of quasi-periodic oscillations (QPOs), fluctuations with a preferred frequency (the centroid frequency of the peak). Usually, the term QPO is reserved for approximately symmetric peaks whose relative width (FWHM [full width at half maximum]/centroid frequency) does not exceed 0.5, and broader features are termed noise, even if the power spectrum has a local maximum (this is sometimes called 'peaked' noise); however, there are no hard and fast rules for this. The width of a QPO peak is a measure for the coherence time of the quasi-periodic signal. The reason that coherence is lost after this time may be, for example, frequency shifts or phase jumps in a persistent signal, or a finite lifetime of an otherwise strictly periodic signal.

Aperiodic X-ray intensity variations bear a close relation both in general aspect and in probable underlying physics to rapid rotation-frequency fluctuations in accreting pulsars. These are caused by fluctuations in the torque exerted by the accreting matter upon the neutron star, and perhaps originate in similar irregularities in the accretion flow that cause the X-ray intensity variations (van der Klis 1995).

Observations of X-ray binaries show variability across a wide range of wavelengths and time scales. The study of this variability is called "timing." For over 30 years, astronomers have contended that clumps of matter orbiting in an accretion disk around a black hole could cause QPOs on the time scale of milliseconds. Since then, the existence of millisecond QPOs has been discovered by *RXTE*. With its large collecting area and microsecond timing resolution, *RXTE* has gathered a flood of timing information that has been only partially analyzed. Our goal is to analyze more of this available data in an attempt to gain insight into what modulates the X-ray flux in QPOs.

1.5 Models

When frequencies are involved, the most obvious potential source of periodic (or quasi-periodic) oscillations is found in the acrretion disk. Particles of matter within the disk follow Keplerian orbits based on radial distances from the black hole. Hence, an initial idea is to test whether QPO frequencies correspond to Kelperian orbital frequencies.

Figure 1-7 gives a schematic represenation of the region near a black hole. The basic concept is that a black hole is surrounded by a hot inner accretion flow from an optically-thick accretion disk. The hot flow constitutes the base of the jets or a hot corona surrounding the black hole. The disk is truncated far away from the innermost stable circular orbit (ISCO). Emission from the hot flow is Compton-upscattered by the hot corona/jets or reflected by the irradiated disk. Soft photons from the cooler accretion disk are also Compton-upscattered by these hot, active regions above the disk. In the end, the X-rays we observe in the lightcurve are a combination of direct emission from the active regions and reflected photons from the accretion disk.

This basic disk plus corona model allows for a hot inner accretion disk whose high temperatures give rise to multiple blackbody components, likely $\sim$1-2 keV, as described by the multi-color disk model (see Mitsuda et al. 1984). Such a hot inner disk ($\sim$10 million K) could serve as a source of soft-seed photons that, when passing through the hotter corona or jets, could be upscattered to higher energies. However, this process can account for only a continuous source of soft-seed photons; it cannot by itself account for QPO behavior.
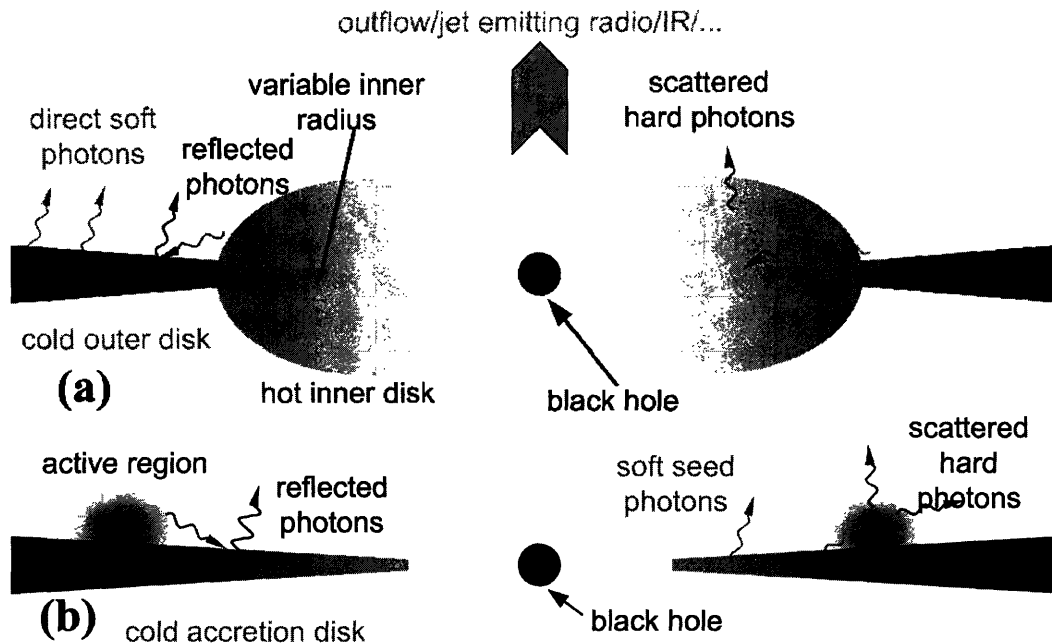
Figure 1-7: (a) A schematic representation of a hot inner accretion flow surrounded by an optically-thick accretion disk. The hot flow constitutes the base of the jet or a hot inner corona surrounding the compact object. The disk is truncated far away from the innermost stable circular orbit (ISCO). Emission from the hot flow is Compton-upscattered by the hot corona/jets or reflected by the irradiated disk. Geometric changes in the disk would change the reflector area, thereby giving rise to variations in observed intensity and energy. (b) A schematic representation of hot, active regions above an optically-thick accretion disk extending close to the ISCO. Changes in the hot, active regions (e.g., corona or jets) would change the intensity of radiation incident upon the disk, therby resulting in variations in observed intensity and energy. (Diagram from Zdziarski and Gierliński (2004).)

Nevertheless, it is a source of X-rays that undoubtedly plays a role in the production of QPOs.

1.6 XTE J1550-564

The X-ray binary XTE J1550−564 was discovered with the *Rossi X-ray Timing Explorer (RXTE)* on September 6, 1998, during the early phase of an outburst. Since then, considerable work has been done to determine the parameters of the system. The mass of the compact object in XTE J1550−564 has been constrained via optical work to $M_1 > 7.4 \pm 0.7 M_\odot$. Recent work has determined that the most likely mass of the black hole in XTE J1550−564 is around 10 $M_\odot$, with a 3 σ range of $7.50 \leq M_1 \leq 13.18 M_\odot$. Analysis of its spectrum over all wavelengths reveals that the emission from XTE J1550−564 is primarily in the X-ray band. The donor star is most likely an evolved subgiant or giant with spectral classification G8 IV to K4 III. The binary system is an LMXB with a mass ratio ($Q \equiv M_1/M_2$) of $6.7 \leq Q \leq 11.0$, an inclination of around 72°, an orbital period of about 1.54 days, an orbital separation near 12 $R_\odot$, and a distance from earth of about 6 kpc (Orosz et al. 2002).

Since its discovery by *RXTE* in 1998, XTE J1550−564 has undergone four outbursts. During its initial outburst from September 1998-May 1999, the source exhibited a flare that reached 6.8 crab at 2-10 keV (Sobczak et al. 2000). It also revealed X-ray QPOs from ∼0.1

Hz to $\sim$270 Hz (Remillard et al. 2002), making it one of only a few galactic black holes known to exhibit QPOs above 50 Hz. Both optical (B$\sim$22 magnitude, see Orosz et al. (1998)) and radio (see Campbell-Wilson et al. 1998) counterparts of XTE J1550$-$564 have been identified. Both X-ray jets (Corbel et al. 2002) and radio jets with apparent superluminal velocities ($> 2c$) have been observed (Hannikainen et al. 2001). X-ray variability has been observed in the range of $\sim$1-15% rms (Cui et al. 1999).

Phase lags and coherence measures of low-frequency QPOs ($\nu < 20$ Hz) are used to classify QPO behavior into three types (see Remillard et al. 2002). Q-values, defined as the centroid frequency divided by the full width at half maximum (FWHM), aid in the classification. Type "A" QPOs are broad (Q$\sim$2-4) features with small rms amplitude ($\lesssim$ 4%) and poor coherence ($< 50\%$). They exhibit large phase lags ($\sim$1 rad) in soft X-rays. Type "B" QPOs are narrow (Q$\sim$4) features with moderate rms amplitude ($\sim$4-6%) and strong coherence ($> 90\%$). They exhibit hard lags ($\lesssim 0.4$ rad) in the strongest feature but soft phase lags in the harmonics. The most common type of QPO, type "C," have sharp ($Q > 10$) fundamental feautures with a range of rms amplitudes ($\sim$3-16%) and strong coherence ($\sim$85-95%). The first harmonic (and usually the first subharmonic) is present. Phase lags are modest, as the fundamental shows soft lags ($|\delta\phi| \lesssim 0.4$ rad). Type "C" QPOs are the best to study because they are the slowest, strongest, and most coherent QPOs of the three. For the XTE J1550$-$564 observations in our study, the QPOs are of type "C."

Chapter 2

Observations and Analysis

The goal of our work was to investigate the connection between the temporal and spectral properties of XTE J1550−564. By comparing the spectra of the source when it is in the *high* intensity phase with the *low* intensity phase of its QPO cycle, we hoped to gain insight into the cause of QPOs and how they relate to structures and processes in the vicinity of black holes. A few methods were available to help us accomplish this. First, using a technique similar to that of Miller and Homan (see Miller and Homan 2005), we could have measured the average flux and then selected periods when the flux was a certain percentage above or below the mean. Second, we could have simply selected a certain percentage of the highest and lowest data points. Third, we could have used folding techniques to determine *high* and *low* flux periods based on the phase of the QPO. Finally, if all else failed, we could have identified all local extrema in the lightcurve, excluded max/min pairs whose difference in count rate fell below a certain separation, excluded max/min pairs that occurred before a complete QPO cycle, and then selected the remaining extrema along with a specific interval on either side.

Because of the rapidly-varying changes in flux between the *high* and *low* intensity phase of the QPO, we were unable to use the technique of Miller and Homan (see Miller and Homan 2005). In other words, the periods of *high* and *low* flux could not be separated effectively by the mean flux. The second option of making simple selections of the highest and lowest certain percentage of data points proved inadequate for the same reason. Because of the variations in amplitude of the flux, periods that were obviously in the *low* flux of the QPO cycle sometimes had higher flux values than periods that were obviously in the *high* flux of the cycle. With regard to folding the data, all attempts failed because phase changes occurred too frequently to identify start and end points for complete cycles. In the end, only careful selection of maxima and minima would suffice.

In this chapter, we describe our methods and techniques used to select and analyze the data. We began by making time selections that correspond to the *high* and *low* intensity phases of the QPO. Next, we used those selected times to extract spectra corresponding to the *highs* and the *lows*. We then obtained spectral fits, which we could then compare to each other as well as to the spectral fit of the average. Finally, we constructed plots of the ratios (*low/high*) of the counts to study the variability. Our results then contained both temporal as well as spectral information about the source.

2.1 Time Selections

In order to observe and analyze the QPOs, we needed slow QPOs with many counts and high rms amplitudes. Slow QPOs were necessary because the QPOs must compete with Poisson noise. Fast QPOs require smaller time bins, resulting in smaller counts. Hence, Poisson noise becomes more important. Slow QPOs allow larger time bins and larger counts, which lowers the relative Poisson error. Furthermore, large amplitudes make differences in *high* and *low* intensity more apparent. Thus, we made power density spectra (PDS) of the X-ray flux in the 3.4-13 keV range from each observation using all available data, and fit the 0.01-100 Hz range with Lorentzian functions in the $\nu-$max representation. A single QPO is the dominant peak in each PDS (see Figure 2-1). These QPO frequencies (ranging from 0.1-4 Hz) along with corresponding observation numbers, dates, Q-values, and rms amplitudes are provided in the table below (see Table 2.1). Q-values are defined by QPO frequency/FWHM. Over 200 observations were available for this source during its major outburst of 1998-1999, but we limited our study to 13 observations at the beginning of the outburst (see Table 2.2). Observation times ranged from 1.1 to 5.7 ks.
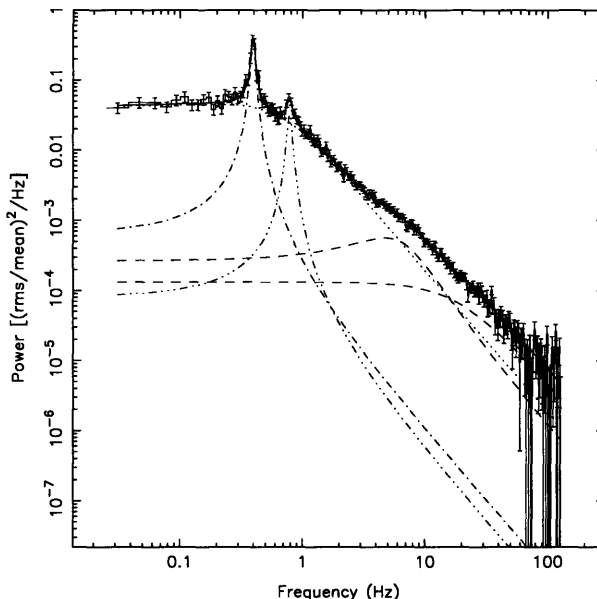
Figure 2-1: Power density spectrum (PDS), showing the clearly visible QPO and its first harmonic.

Analysis of power density spectra made from the initial observations of the 1998 outburst resulted in strong QPOs in the range of 0.1-4 Hz. These QPO frequencies along with corresponding Q-values served two purposes. First, they were used to determine the appropriate size of our time bins for each observation (see Table 2.2). Data extraction with these time bins yielded a target of 16 selected data points per QPO cycle. Second, they defined the intervals around each QPO frequency used by the band-pass filter to exclude high-frequency and low-frequency noise.

We defined basic good time interval (GTI) files based on our analysis of each observation's filter file. For each observation, we ensured that data were taken only from times when the maximum number of PCUs were on. All but three observations used all 5 PCUs for the majority of the available observation time. In the third, sixth, and eleventh obser-

Obs.	Obs. ID	Date (MJD)	Freq (Hz)	Q-value	rms (%)
1	30188-06-03-00	51064.01	0.122(1)	6(1)	14.9(8)
2	30188-06-01-00	51065.07	0.290(1)	11(2)	14.8(6)
3	30188-06-01-01	51065.34	0.395(2)	12(2)	13.7(6)
4	30188-06-01-02	51066.07	0.809(3)	13(2)	13.4(7)
5	30188-06-01-03	51066.35	1.035(3)	11.2(8)	15.1(3)
6	30188-06-04-00	51067.27	1.544(3)	9(1)	15.7(3)
7	30188-06-05-00	51068.35	2.392(4)	11(1)	14.5(2)
8	30188-06-06-00	51069.28	3.332(5)	12.0(5)	13.6(2)
9	30188-06-07-00	51070.13	3.193(4)	13.5(4)	13.7(2)
10	30188-06-08-00	51070.28	3.174(4)	14.1(6)	13.7(2)
11	30188-06-09-00	51071.20	3.665(4)	13.5(5)	13.3(2)
12	30188-06-10-00	51072.00	2.575(4)	18(2)	13.9(4)
13	30188-06-11-00	51072.35	4.006(5)	14.2(6)	12.9(2)

Table 2.1: Log of observations, observation id numbers, dates, QPO frequencies, Q-values, and rms. Q-values are defined by QPO frequency/FWHM.

Obs.	QPO Frequency	Binsize (s)	Bins/QPO Cycle
1	0.122(1)	0.5	16.4
2	0.290(1)	0.21875	15.8
3	0.395(2)	0.15625	16.2
4	0.809(3)	0.0625	19.7
5	1.035(3)	0.0625	15.5
6	1.544(3)	0.03125	20.7
7	2.392(4)	0.03125	13.4
8	3.332(5)	0.03125	9.6
9	3.193(4)	0.03125	10.0
10	3.174(4)	0.03125	10.2
11	3.665(4)	0.03125	8.7
12	2.575(4)	0.03125	12.4
13	4.006(5)	0.03125	7.8

Table 2.2: Log of observations, QPO frequencies, binsizes, and the number of bins per QPO cycle.

vations, the maximum number of PCUs available for the majority of the observation times were 3, 4, and 3 PCUs respectively. To avoid any earth occultations, we ensured that the elevation angle of the detector (relative to the horizon) was greater than 10°. Since the rocking motion of HEXTE sometimes induces a small amount of slew that makes the pointing unstable, we filtered out pointings with offset greater than 0.02°. When the satellite passes through the South Atlantic Anomaly (SAA), the background increases dramatically. We negated this effect by requiring the time since SAA passage to be greater than 20 minutes. Electron contamination was not an issue since XTE J1550−564 is a bright X-ray source.

The data collection modes used during this time period included the b-mode (binned) and the ev-mode (event). Data from observation 30188-06-02-00 were corrupted (count rates

were too high for the data mode), so we excluded the observation from our study. The data for our analysis came from the "B_4ms_8A_0_35_H" mode data from each observation (except the first, which used the "B_8ms_16A_0_35_H_4P" mode data) and the "E_16us_16B_36_1s" mode data from each observation (except the first, which used the "E_62us_32M_36_1s" mode data).

The binned-mode data had a time resolution of 4 ms (2^{-8} s) with 8 energy channels (except for the first observation, which had a time resolution of 8 ms (2^{-7} s) with 16 energy channels). The event-mode data had a time resolution of 16 μs (2^{-16} s) with 16 energy channels (except the first observation, which had a time resolution of 62 μs (2^{-14} s) with 32 energy channels). The two standard modes (standard-1 and standard-2), providing 1/8 s timing in one energy band and 16 s timing in 129 channels respectively, were available throughout all the observations.

Lightcurves from all channels of the b-mode data were used to determine the *high* and *low* intensity data points. These lightcurves were extracted with the ftool "saextrct" using time bins with target sizes equal to 1/16 of the QPO period. However, "saextrct" requires the binsize to be integer multiples of each data mode's intrinsic time resolution, so the binsizes had to be adjusted accordingly. For each observation, after determining the value of 1/16 of the QPO period, the binsize was adjusted to reflect the closest common multiple of the intrinsic timing resolution of both the b-mode and ev-mode. For example, the first observation gave a target binsize of 0.5110 seconds. The b-mode resolution was 8 ms (2^{-7} s) while the ev-mode resolution was 62μs (2^{-14} s). The closest common multiple of these two modes was 0.5 seconds. The binsizes for each observation and the corresponding number of bins per QPO cycle are given in Table 2.2.

In order to filter out both low frequency and high frequency noise, the b-mode light curve was passed through a band-pass filter using the "digital_filter" command in IDL Version 6.0.3. The center of the band-pass was set by the QPO frequency. The width of the band-pass was set by the FWHM obtained from the Lorentzian functions of the QPO frequencies and their Q-values (see Table 2.1). The width of each band-pass ranged from about 0.0032 Hz to 0.28 Hz. The filtered lightcurve was then obtained by using the "convol" command in IDL to convolve the original count rate with the digital filter (see Figure 2-2).

The search for *high* and *low* data points involved identifying the times corresponding to the local maxima and minima in the filtered lightcurve (see the build_histo code). Once this was accomplished, a histogram was generated containing the differences in count rate between each maximum/minimum pair (see Figure 2-3). A threshold limit of 75% of the mode difference (the difference in count rate with the highest number of occurrences) was used to exclude pairs representing only partial cycles. An additional requirement was imposed that excluded any adjacent maxima or minima that were not separated by at least 6 time bins (roughly 1/3 of the QPO period) (see the find_extrema code). Upon final identification of qualifying extrema, the times corresponding to the data points on either side of the selected extrema were added to the time selections, thereby ensuring a selection rate of 6 time bins per period. These groups of 3 consecutive time bins formed the new *high* and *low* intensity time stamps from which spectra from the original unfiltered data could be extracted. Although the goal was to select 6 out of 16 time bins per period, observations 7 through 13 had less than 16 total time bins per QPO period (see Table 2.2). For some unknown reason, "saextrct" will not properly process time bins that are smaller than 0.03125 seconds, even when the time bins are expressed in integer multiples of the data mode resolution.
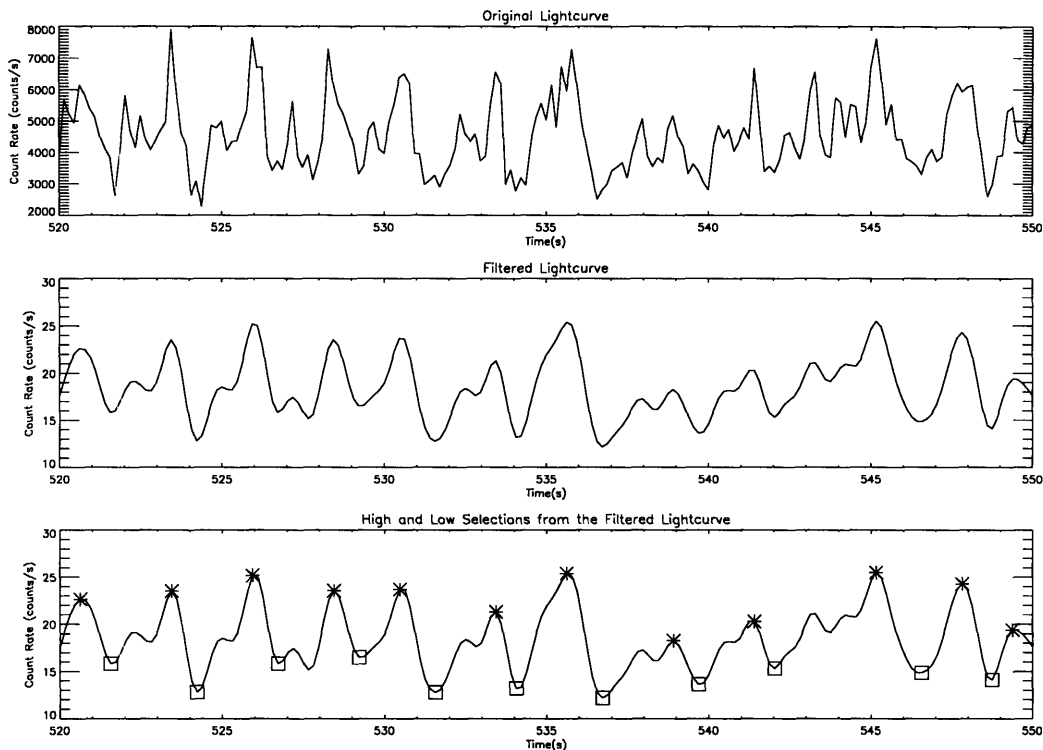
Figure 2-2: The first plot shows 30 seconds of data from the original lightcurve of observation 3. The second plot shows the same 30 seconds of data after the low-frequency and high-frequency noise were filtered. The third plot shows the selections of *high* (asterisks) and *low* (boxes) data points based on the selection criteria. As part of the selection process, the data points on either of side of each maximum and minimum were included to ensure the selection of 6 data points per QPO cycle.

2.2 Spectra

Extraction of spectra for the *high* and *low* intensity phases of the b-mode and ev-mode of each observation was accomplished using the ftools "saextrct" and "seextrct" respectively. Text files containing the previously-obtained time markers corresponding to the extrema were used as input for time interval selections in the extraction tools.

After extraction, the spectra were reduced according to data reduction procedures from the *RXTE Cook Book*. The spectral data were corrected for deadtime in accordance with "Correcting for PCA Deadtime." Background files were generated according to "Using the Latest Pcabackest" using the PCA Background model.[1] Response matrices were created using "Creating PCA Responses."

For the purpose of determining ratios of *low* counts/*high* counts, a systematic error of 0.2% was applied to the total number of counts in each bin for all spectra. To accurately estimate *relative* differences in flux acquired with the same detector, what is important is understanding the degree to which systematic errors may *change* over time. To this end, we reduced and analyzed spectra from the Crab Nebula over a timescale of months. Absorbed power law fits to these spectra revealed that most channels differ by 0.2% or less. To be conservative, we added 0.2% systematic errors to the spectra for the determination of ratios

---

[1]For our analysis, we used the file "pca_bkgd_cmbrightvle_eMv20020201.mdl."

31
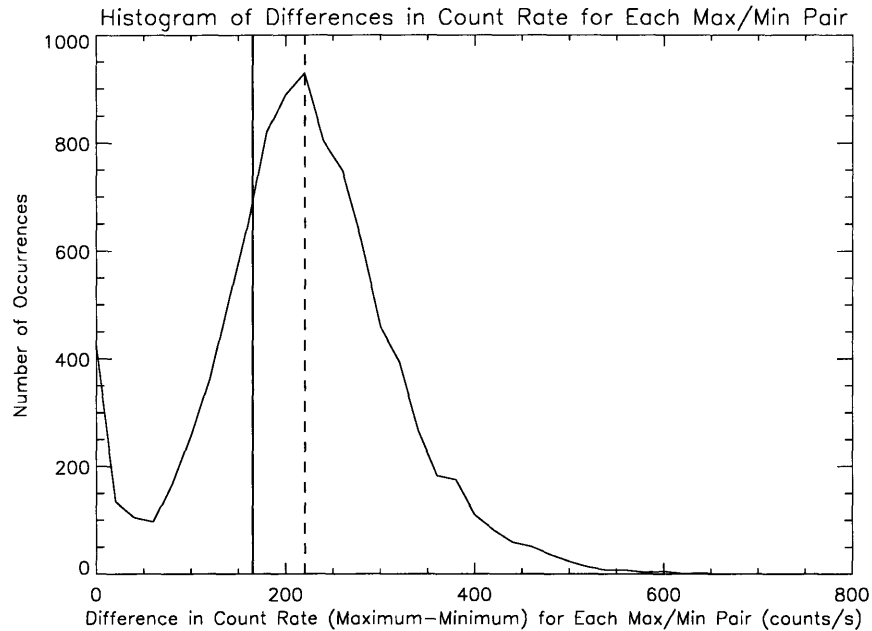
Figure 2-3: Histogram of differences vs. occurrences for observation 10, showing the differences in count rate between each maximum/minimum pair. For each maximum/minimum pair, if the difference was less than 75% of the mode difference, then the data points were rejected. In this case, the mode difference was 220, so maximum/minimum pairs whose difference was less than 165 were rejected.

of *low* counts/*high* counts even though the timescale of our observations was only eight days. However, to avoid over-constraining the spectral fits, we chose a systematic error of 0.5% to apply to the spectra when conducting spectral fitting.

Spectral analysis was performed using XSPEC Version 11.3.0. A spectral fit was obtained for each observation by analyzing the standard-2 data as an average of the entire observation. The background was subtracted from each standard-2 spectrum, and the analyzed data were restricted to the energy range 2.8-25 keV. This selection of energy range resulted in analysis of 7 out of 8 channels in the b-mode, and 9 out of 15 in the ev-mode. The first observation had twice the energy resolution, resulting in analysis of 15 out of 16 channels and 9 out of 32 channels respectively.

The first fit to be obtained for each spectrum was one using a phenomenological model consisting of absorption of a broken power law and a Gaussian. The Gaussian peaked at 6.4 keV, signifying the Fe Kα emission line. Once a fit was obtained for the average spectra (using the standard-2 data), the same parameters were applied to the *high* and *low* intensity spectra. Only the broken power law normalization and the Gaussian normalization were allowed to vary for the initial fit. Then the broken power law indices were allowed to vary in order to get a better fit. The *high* and *low* intensity spectra could then be compared with regard to the average spectra.

The second fit obtained for each spectrum was one based on a physical model using absorption of a Gaussian and a reflection model called "pexrav" (Magdziarz and Zdziarski 1995). The pexrav model is an exponentially cut off power law spectrum "reflected" (i.e., incident photons are scattered and reprocessed) from neutral material. The output spectrum is the sum of the cut-off power law and the reflection component. The model was first

applied to the average spectra in order to determine initial parameters for the average. These parameters for the average were then applied to the *high* and *low* intensity spectra. Only the Gaussian line energy and width were kept frozen. The resulting resulting spectra could then be compared to the average.

2.3 Ratios

Ratios of counts (*low/high*) convey valuable information about variability. The ratios specify a direct measure of the difference between the *low* intensity and the *high* intensity of the QPO phase. In effect, the ratios give a direct measure of the amplitude of the QPO, and, therefore, its rms. Additionally, the ratios can reveal any existing correlations between QPO frequency and energy.

To construct ratio plots, the binned-mode counts were combined with the event-mode counts for the *highs* and then for the *lows*, omitting the first value in the binned-mode data (corresponding to channel 1) and the last 4 values in the event-mode data (corresponding to channels with energies over about 31 keV). Since each energy channel covers a range of energies, we used the average energy of each bin as the energy value for the entire bin. Hence, we were then able to establish a one-to-one assignment of energy for each count rate.

Chapter 3

Results

The QPO frequencies in our sample were strongly correlated with the overall source flux (see Cui et al. 1999). This correlation is readily apparent in Figure ?? and Figure ??. The QPOs varied between 0.1 and 4 Hz. The rms amplitude ranged from ~13-16%, and Q-values ranged from ~6-18 (see Figure 3-3).
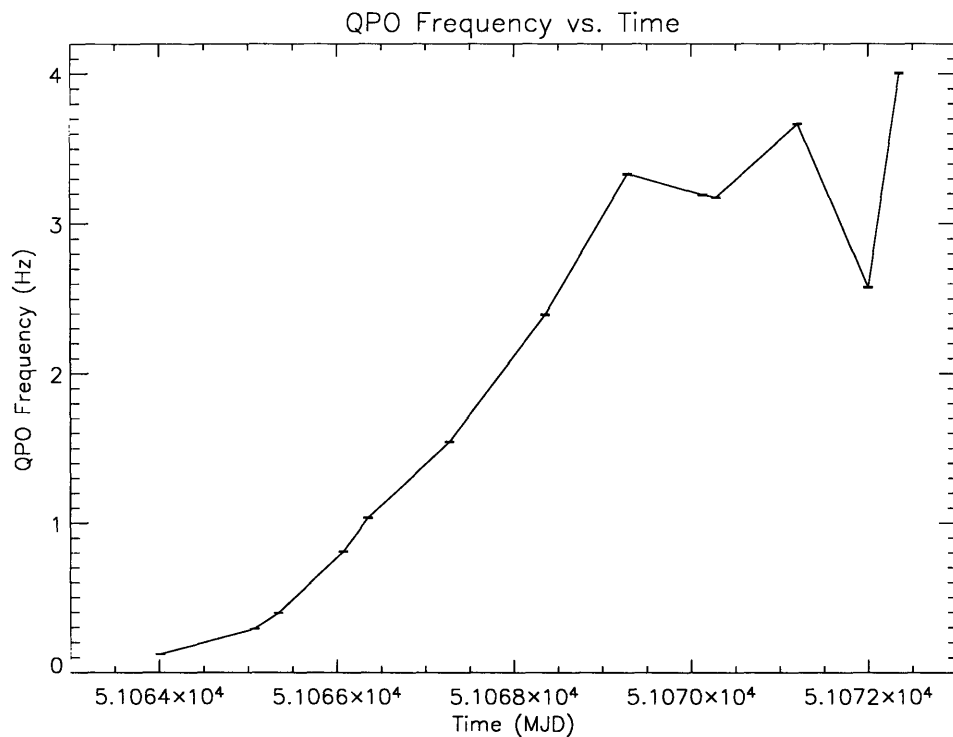
Figure 3-1: Plot of QPO frequency vs. time.

Differences in count rate between maxima and minima in the filtered light curves ranged from values consistent with zero to ~1100 counts/s. A histogram of the data selections from each observation yielded the necessary cutoff points that would exclude any two maxima whose difference fell below 75% of the mode difference (the difference with the highest number of occurrences, see Figure 2-3). Additionally, requiring the time interval between consecutive maxima or minima to be at least 6 times the binsize excluded all "false" cycles
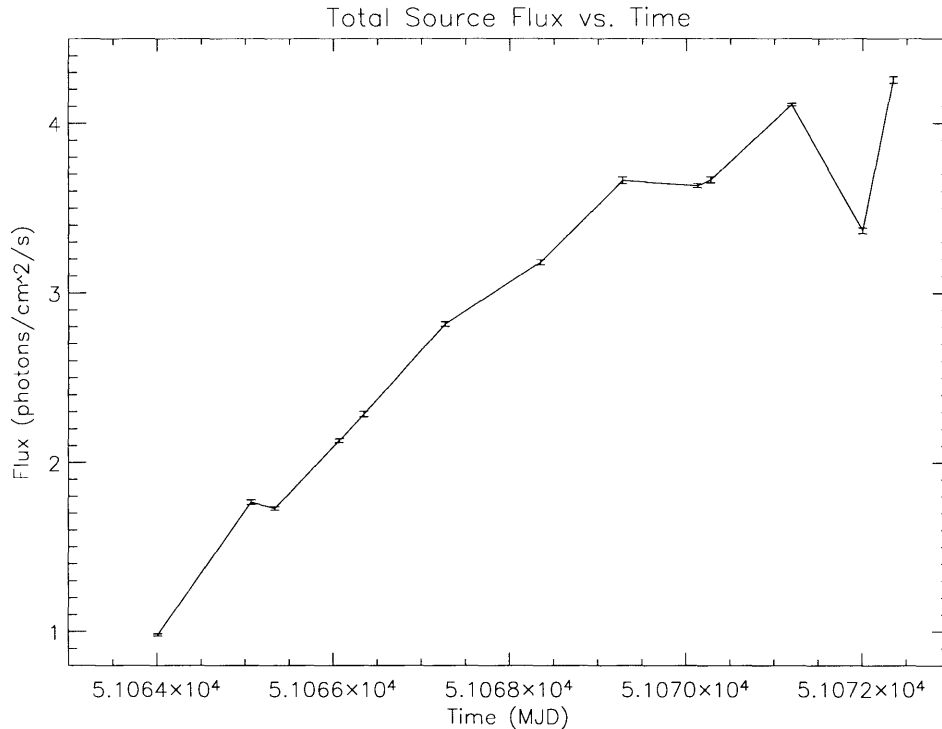
Figure 3-2: Plot of the total source flux vs. time.

shorter than roughly one third of the QPO period.

For our initial fit of the spectra in observation 1, we used a phenomenological model consisting of absorption of a broken power law and a Gaussian (see Figure 3-4 and Figure 3-5). After obtaining good fits to the spectra in observation 1, we again applied the model to observations 2. Analysis of the resulting spectral fits revealed that in both intensity levels, the Fe Kα line showed no significant change in equivalent width (within measurement errors) (see Table 3.1 and Table 3.2). However, a correlation between the Fe Kα line and the continuum was observed. The flux of the Fe Kα line rose and fell at the same rate as the continuum flux (within measurement errors). In other words, the relative contribution from the Fe line to the overall flux did not change (see Table 3.1 and Table 3.2). Observations 1 and 2 allowed us to see evidence for this correlation between the Fe Kα line and the intensity of the continuum, which is modulated by the QPO frequency. Meanwhile, the broken power law showed no significant change (within measurement errors).

The first observation, by virtue of its improved energy resolution over the remaining observations, led us to attempt a second fit using an alternative model. In our second attempt, we obtained another good fit from the average spectra using a physical model comprised of absorption of a Gaussian and the "pexrav" reflection model (Magdziarz and Zdziarski 1995) (see Figure 3-6 and Figure 3-7). Again, the Gaussian again peaked at 6.4 keV, signifying the Fe Kα emission line. Analysis of the resulting spectral fits for observation 1 again revealed no significant change in equivalent width of the Fe Kα line (within measurement errors). Furthermore, the flux of the Fe Kα line rose and fell at the same rate as the continuum flux (within measurement errors), meaning that the relative contribution from the Fe line to the overall flux did not change. The reflection indices, on

36

Parameter	Average	High	Low	Ratio (high/low)
N_H	0.9	0.9	0.9	
Γ_1	1.611(4)	1.621(4)	1.603(4)	
E_{Br}	$10.89^{+0.08}_{-0.3}$	10.8860	10.8860	
Γ_2	$1.384^{+0.007}_{-0.002}$	1.499(6)	1.354(7)	
K_{pl}	1.54(1)	2.20(2)	1.085(8)	
E_g	6.40(2)	6.4	6.4	
σ_g	0.76(8)	0.76	0.76	
K_g	$0.012^{+0.0011}_{-0.0008}$	0.016(1)	0.0089(6)	
EW_g	154	149	160	
χ^2/dof	0.75/46	1.03/20	1.37/20	
F_{pl}		1.830(13)	0.957(8)	
F_{pl} ratio				1.91(2)
F_g		0.0163(11)	0.0089(6)	
F_g ratio				1.83(18)

Table 3.1: Parameter changes in the spectral fits for the average, high, and low spectra of observation 1 using the "phenomenological" model of a power law and a Gaussian. N_H is the equivalent hydrogen column in units of 10^{22} atoms/cm^2. E_{Br} is the break point for the energy in keV. Γ_1 is the power law photon index for E $< E_{Br}$. Γ_2 is the photon power law index for E $> E_{Br}$. K_{pl} is the normalization in photons/keV/cm^2/s at 1 keV. E_g is the Gaussian line energy in keV. σ_g is the line width in keV. K_g is the line normalization in total photons/cm^2/s. EW_g is the line equivalent width in eV. $\chi^2/$dof is the reduced χ-squared of the fit and the number of degrees of freedom. F_{pl} is the broken power law flux in photons/cm^2/s. F_g is the line flux in photons/cm^2/s. Where errors are not given, the parameter was fixed. In the case of the line equivalent width, XSPEC does not compute the error, so we took it to be the error in the line normalization. In determining the fluxes, XSPEC could not compute the error because of fixed parameters, so we took it to be the error in the broken power law normalization and the line normalization.

Parameter	Average	High	Low	Ratio (high/low)
N_H	0.9	0.9	0.9	
Γ_1	1.677(5)	$1.47^{+0.17}_{-1.0}$	1.693(16)	
E_{Br}	$9.3^{+0.7}_{-1.0}$	$3.6^{+1.2}_{-0.6}$	8.7(13)	
Γ_2	1.630(3)	1.688(10)	1.607(11)	
K_{pl}	3.16(2)	$3.7^{+0.8}_{-0.5}$	2.39(5)	
E_g	6.40(1)	6.4	6.4	
σ_g	0.88(6)	$0.73^{+0.15}_{-0.4}$	0.7(8)	
K_g	0.034(2)	0.039(10)	0.023(3)	
EW_g	242	184	216	
χ^2/dof	3.88/46	0.93/9	2.12/9	
F_{pl}		3.4(6)	1.73(3)	
F_{pl} ratio				2.0(4)
F_g		0.039(10)	0.023(3)	
F_g ratio				1.7(5)

Table 3.2: Parameter changes in the spectral fits for the average, high, and low spectra of observation 2 using the "phenomenological" model of a power law and a Gaussian. N_H is the equivalent hydrogen column in units of 10^{22} atoms/cm^2. E_{Br} is the break point for the energy in keV. Γ_1 is the power law photon index for E $< E_{Br}$. Γ_2 is the photon power law index for E $> E_{Br}$. K_{pl} is the normalization in photons/keV/cm^2/s at 1 keV. E_g is the Gaussian line energy in keV. σ_g is the line width in keV. K_g is the line normalization in total photons/cm^2/s. EW_g is the line equivalent width in eV. $\chi^2/$dof is the reduced χ-squared of the fit and the number of degrees of freedom. F_{pl} is the broken power law flux in photons/cm^2/s. F_g is the line flux in photons/cm^2/s. Where errors are not given, the parameter was fixed. In the case of the line equivalent width, XSPEC does not compute the error, so we took it to be the error in the line normalization. In determining the fluxes, XSPEC could not compute the error because of fixed parameters, so we took it to be the error in the broken power law normalization and the line normalization.

Figure 3-3: Frequencies, Q-values (a), and rms (b), obtained from the Lorentzian function corresponding to each QPO.

the other hand, revealed a decrease from the average in the *high* intensity spectra and a small increase from the average in the *low* intensity spectra (see Table 3.3). Within measurement errors, no significant changes in power law indices were observed.

Both models show that, in observation 1, the Fe Kα line flux increases from the average in the *highs* and decreases from the average in the *lows*, but the equivalent width remains constant (within errors) (see Table 3.1 and Table 3.3). In the reflection model, the reflection fraction decreases from the average in the *highs* and increases from the average in the *lows* (see Table 3.3). We attempted to apply the pexrav model to later observations, but we could not get a reduced χ^2 per degree of freedom (dof) better than 2.48(47) even when applied to the average spectra.[1]

Spectral fitting of observations 3-13 required an additional model component to achieve good fits for the average spectra (see Table 3.4). In the case of observation 3, the addition of an absorption edge ~9 keV improved the reduced χ^2 per degree of freedom (dof) from 3.79(46) to 0.44(44). The remaining observations showed the same effect, so we applied an absorption edge to the model components in all subsequent observations. We judged that the edge occurred at a sufficiently high energy to have only minimal impact on the Fe Kα line. For our purposes, the edge would not affect our ability to compare Fe line strengths found at lower energies.

---

[1] χ^2 here is the reduced χ^2 defined by χ^2/dof. Degrees of freedom (dof) are annotated in parentheses.

Parameter	Average	High	Low	Ratio (high/low)
N_H	0.9	0.9	0.9	
E_g	6.40(3)	6.4	6.4	
σ_g	$1.36^{+0.12}_{-0.07}$	1.36	1.36	
K_g	$0.0179^{+0.0017}_{-0.0009}$	0.023(2)	0.0129(9)	
Γ	1.666(6)	1.641(7)	1.664(8)	
E_c	200	200	200	
rel_refl	$0.82^{+0.04}_{-0.02}$	0.46(3)	0.88(5)	
K_{pl}	1.62(1)	2.24(2)	1.16(1)	
EW_g	228	208	229	
χ^2/dof	0.98/47	1.25/19	1.67/19	
F_{pl}		1.829(18)	0.960(12)	
F_{pl} ratio				1.90(3)
F_g		0.0227(16)	0.0129(9)	
F_g ratio				1.76(17)

Table 3.3: Parameter changes in the spectral fits for the average, high, and low spectra of observation 1 using the "physical" model of a Gaussian and a pexrav reflection model. N_H is the equivalent hydrogen column in units of 10^{22} atoms/cm^2. E_g is the Gaussian line energy in keV. σ_g is the line width in keV. K_g is the line normalization in total photons/cm^2/s. Γ is the power law photon index. E_c is the cutoff energy in keV. rel_refl is the scaling factor for reflection. K_{pl} is the normalization in photons/keV/cm^2/s at 1 keV for the power law only in the observed frame. EW_g is the line equivalent width in eV. χ^2/dof is the reduced χ-squared of the fit and the number of degrees of freedom. F_{pl} is the power law flux in photons/cm^2/s. F_g is the line flux in photons/cm^2/s. Where errors are not given, the parameter was fixed. In the case of the line equivalent width, XSPEC does not compute the error, so we took it to be the error in the line normalization. In determining the fluxes, XSPEC could not compute the error because of fixed parameters, so we took it to be the error in the power law normalization and the line normalization.

Obs.	Freq.(Hz)	Intensity	Model Components	χ^2(dof)
1	0.122(1)	Average	broken power law + Gaussian	0.75(46)
		High	broken power law + Gaussian	1.03(20)
		Low	broken power law + Gaussian	1.37(20)
		Average	pexrav + Gaussian	0.98(47)
		High	pexrav + Gaussian	1.25(19)
		Low	pexrav + Gaussian	1.67(19)
2	0.290(1)	Average	broken power law + Gaussian	3.88(46)
		High	broken power law + Gaussian	0.93(9)
		Low	broken power law + Gaussian	2.12(9)
3	0.395(2)	Average	(broken power law + Gaussian) × edge	0.44(44)
		High	(broken power law + Gaussian) × edge	0.58(7)
		Low	(broken power law + Gaussian) × edge	1.28(7)
4	0.809(3)	Average	(broken power law + Gaussian) × edge	0.78(44)
		High	(broken power law + Gaussian) × edge	2.09(7)
		Low	(broken power law + Gaussian) × edge	2.00(7)
5	1.035(3)	Average	(broken power law + Gaussian) × edge	0.55(44)
		High	(broken power law + Gaussian) × edge	5.25(7)
		Low	(broken power law + Gaussian) × edge	3.76(7)
6	1.544(3)	Average	(broken power law + Gaussian) × edge	0.89(44)
		High	(broken power law + Gaussian) × edge	3.66(7)
		Low	(broken power law + Gaussian) × edge	7.54(7)
7	2.392(4)	Average	(broken power law + Gaussian) × edge	0.91(44)
		High	(broken power law + Gaussian) × edge	7.42(7)
		Low	(broken power law + Gaussian) × edge	8.28(7)
8	3.332(5)	Average	(broken power law + Gaussian) × edge	1.98(44)
		High	(broken power law + Gaussian) × edge	7.20(7)
		Low	(broken power law + Gaussian) × edge	6.64(7)
9	3.193(4)	Average	(broken power law + Gaussian) × edge	1.58(44)
		High	(broken power law + Gaussian) × edge	7.69(7)
		Low	(broken power law + Gaussian) × edge	9.47(7)
10	3.174(4)	Average	(broken power law + Gaussian) × edge	1.44(44)
		High	(broken power law + Gaussian) × edge	5.72(7)
		Low	(broken power law + Gaussian) × edge	8.35(7)
11	3.665(4)	Average	(broken power law + Gaussian) × edge	1.76(44)
		High	(broken power law + Gaussian) × edge	2.91(7)
		Low	(broken power law + Gaussian) × edge	5.84(7)
12	2.575(4)	Average	(broken power law + Gaussian) × edge	1.61(44)
		High	(broken power law + Gaussian) × edge	4.59(7)
		Low	(broken power law + Gaussian) × edge	3.36(7)
13	4.006(5)	Average	(broken power law + Gaussian) × edge	1.36(44)
		High	(broken power law + Gaussian) × edge	5.59(7)
		Low	(broken power law + Gaussian) × edge	6.97(7)

Table 3.4: Log of the model components used to fit each observation. χ^2 here is the reduced χ^2 defined by χ^2/dof. The degrees of freedom are given by (dof).

Figure 3-4: Example fit of the *high* spectrum for observation 1 using absorption of a broken power law and a Gaussian.
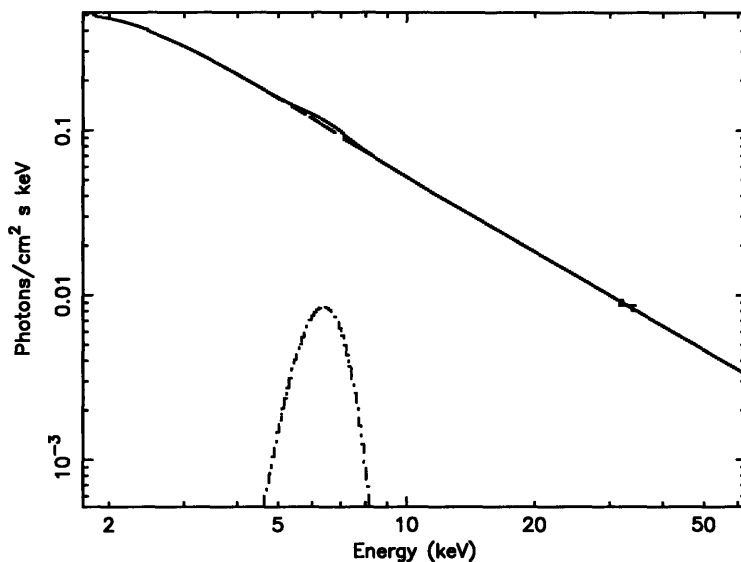
Figure 3-5: Example model for observation 1 using absorption of a broken power law and a Gaussian.

Although this model with the edge gave us good fits for the average spectra in observations 3-13, we were unable to obtain good fits for the *high* and *low* intensity spectra (see Table 3.4). However, most of the residuals occurred at high energies (>10 keV), so our study of the Fe line could still be accomplished. Measurements of the Fe Kα line flux and equivalent width are listed in Table 3.5 along with measurements of the continuum flux. Data from observations 3-13 revealed that the correlation between the Fe Kα line and the continuum (as observed in observations 1 and 2) does not always occur. In fact, between

42

Fit of the Average Spectrum for Obs. 1 Using Pexrav and a Gaussian
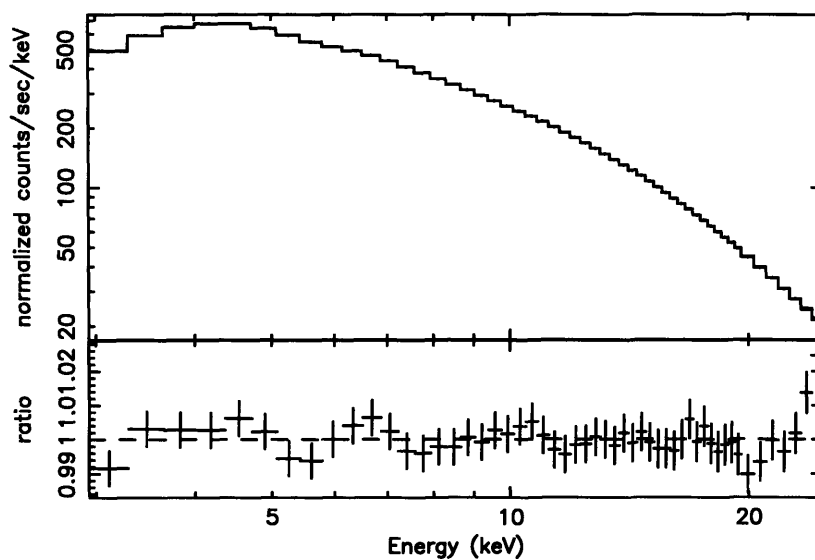
Figure 3-6: Example fit of the average spectrum for observation 1 using absorption of a Gaussian and a "pexrav" reflection model.

observations, the Fe Kα line can change from showing a correlation with the continuum to showing a strong anti-correlation with the continuum. Ratios are provided for comparison between the *high* and *low* intensity phase of each QPO.

Ratios of the continuum flux (*high/low*) are plotted over time in Figure 3-8. Ratios of the Fe Kα line flux (*high/low*) are plotted over time in Figure 3-9. Comparison of only two observations, such as 1 and 2, may suggest a correlation. Comparing 13 observation

Model Using Pexrav and a Gaussian
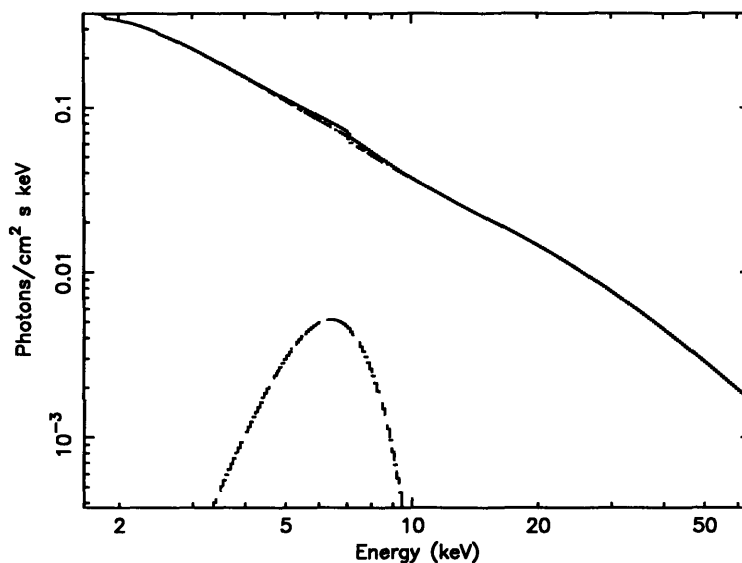
Figure 3-7: Example model for observation 1 using absorption of a Gaussian and a "pexrav" reflection model.

Obs.	Intensity	Continuum Flux	Ratio (H/L)	Fe Line Flux	Ratio (H/L)	EW_g Ratio (L/H)
1	High	1.830(13)	1.91(2)	0.0163(11)	1.83(18)	1.07(10)
	Low	0.957(8)		0.0089(6)		
	High*	1.829(18)	1.90(3)	0.0227(16)	1.76(17)	1.10(11)
	Low*	0.960(12)		0.0129(9)		
2	High	3.4(6)	2.0(4)	0.039(10)	1.7(5)	1.2(3)
	Low	1.73(3)		0.023(3)		
3	High	3.26(10)	1.89(7)	0.012(9)	1.2(9)	1.7(12)
	Low	1.72(3)		0.010(2)		
4	High	4.01(12)	1.94(8)	0.014(6)	0.7(3)	2.9(14)
	Low	2.07(6)		0.020(5)		
5	High	4.31(6)	1.93(3)	0.016(3)	0.81(17)	2.5(5)
	Low	2.23(2)		0.020(3)		
6	High	5.01(5)	1.9(4)	0.151(15)	5.9(6)	0.33(4)
	Low	2.7(5)		0.025(1)		
7	High	5.30(6)	1.72(11)	0.036(4)	1.8(3)	1.02(18)
	Low	3.07(18)		0.020(3)		
8	High	5.54(4)	1.50(1)	0.062(4)	3.0(3)	0.51(5)
	Low	3.697(4)		0.0206(12)		
9	High	5.56(4)	1.52(3)	0.073(4)	3.5(4)	0.44(5)
	Low	3.65(6)		0.021(2)		
10	High	5.60(4)	1.53(2)	0.080(6)	4.0(5)	0.39(4)
	Low	3.66(5)		0.0198(18)		
11	High	6.07(6)	1.44(3)	0.069(9)	6.9(18)	0.21(6)
	Low	4.21(7)		0.010(2)		
12	High	5.45(3)	1.64(7)	0.133(9)	5.3(8)	0.28(4)
	Low	3.32((13)		0.025(3)		
13	High	6.22(6)	1.420(18)	0.029(3)	1.3(4)	1.1(4)
	Low	4.38(4)		0.022(6)		

Table 3.5: Log of fluxes for each observation. Fluxes are in units of photons/cm^2/s. All observations were fit with a broken power law, Gaussian, and absorption edge, with the exception of observations 1 and 2, which were fit without an edge. The entries with asterisks in observation 1 signify fits made using pexrav and a Gaussian.

together, however, we see no apparent correlation between the flux of the Fe line and the flux of the continuum.

On the other hand, a ratio plot of *low* counts/*high* counts for the lowest energy bin revealed a nearly linear relationship between QPO frequency and ratio (and, thus, variability) (see Figure 3-11). All points on the plot fall within 7% of the best-fit line. Ratio plots of all observations together (see Figure 3-10) confirmed that the rms decreases (higher ratio) with QPO frequency. The ratios also showed that the rms increases (lower ratio) with energy up to about 10 keV, above which it decreases slightly (higher ratio). The shape of the ratio curves (ratio vs. energy) at low energies is nearly identical for the later observations (7-13). In other words, the average slope of the ratio curves below 10 keV (slope$\equiv\Delta$ratio/Δenergy) does not change by more than 20% in these observations. By comparison, the average slope of the first 5 observations differs from the average slope of the last 7 observations by ~90%.

Similar to Cui et al. (1999), we found a strong anti-correlation between the frequency of the QPO and its strength. The rms also decreased with QPO frequency. The ratios of the *low* intensity and *high* intensity count rates in the 3.3-31 keV energy range indicate an
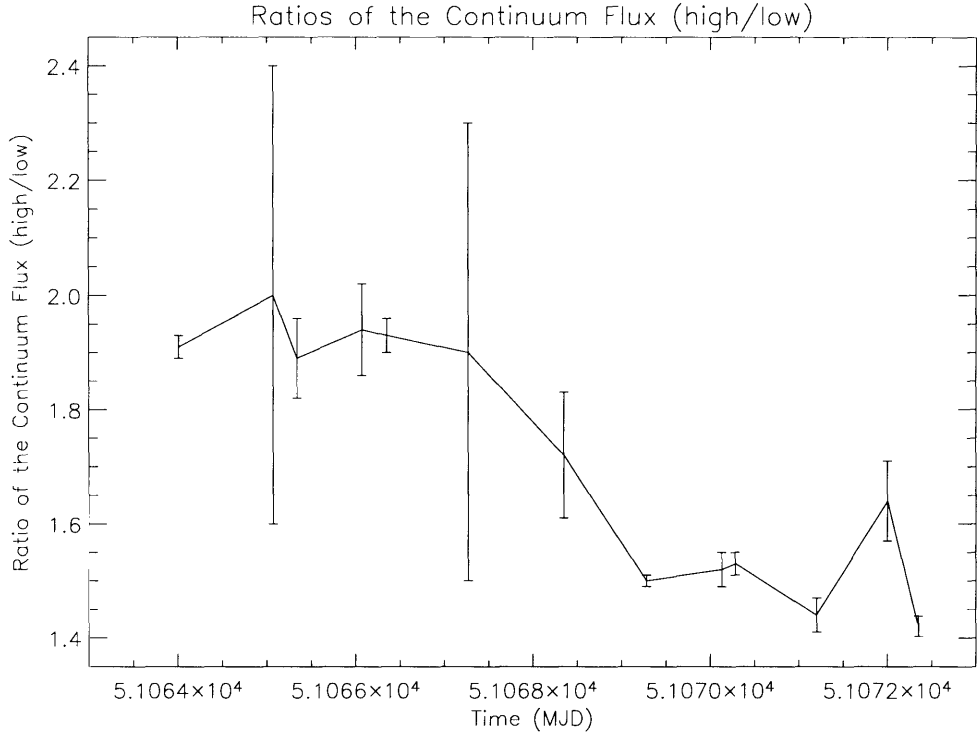
Figure 3-8: The continuum flux, shown as a ratio (high/low) over time.

increase in the QPO strength (lower ratio) up to about 10 keV, above which it decreases only slightly (see Figure 3-10). The change in QPO frequency between observations 6 and 7 is a transition from ~1.5 Hz to ~2.4 Hz (see Table 2.1).

In our observations, the phase lags were very small. The largest was -0.07 rad in observation 13, corresponding to -0.05 seconds in the 4 Hz QPO. The resulting effect is only ~1%, so it is doubtful that any change in our results would have been observed had we applied this phase lag to the data.
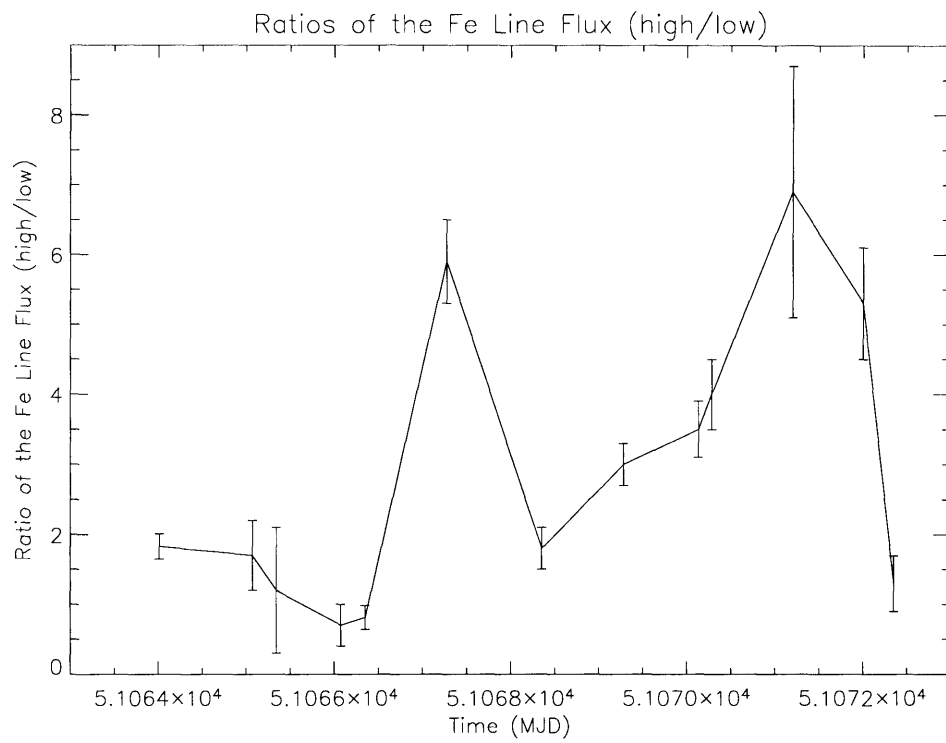
Figure 3-9: The Fe Kα line flux, shown as a ratio (high/low) over time.
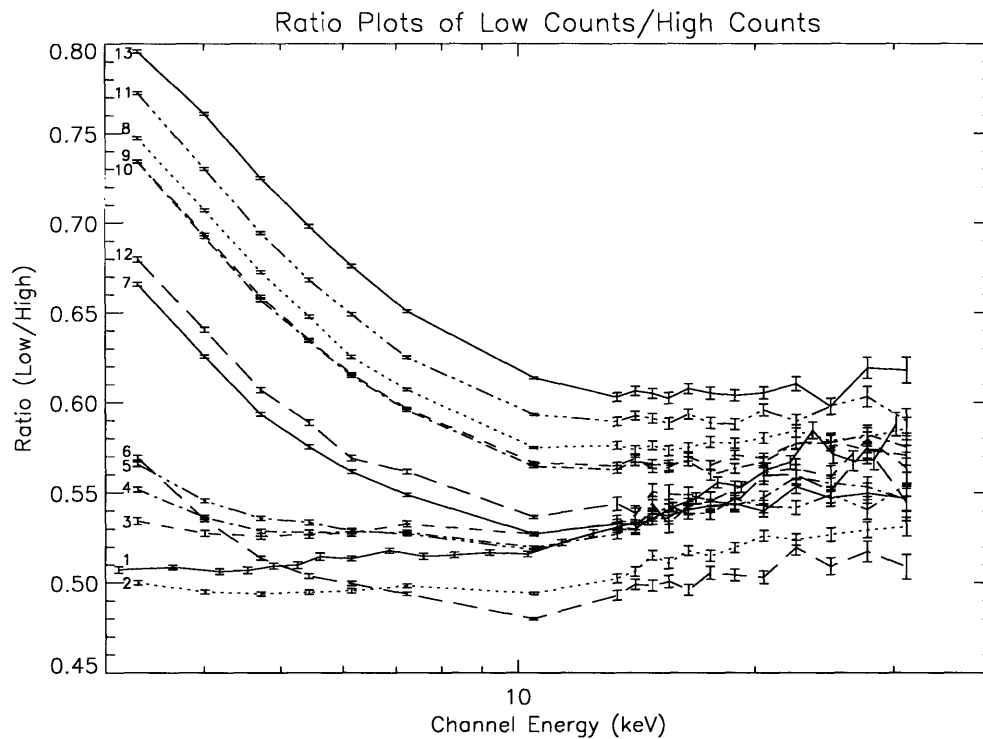
Figure 3-10: Ratio plots of *low* counts/*high* counts for all observations, showing how variability changes with QPO frequency and energy. The observation number is located to the left of its corresponding plot. From the bottom to the top of the picture, the observations are in order of increasing QPO frequency (except observation 1, which is out of order and falls above observation 2 even though it has the lowest QPO frequency, as evidenced in Figure 3-11).
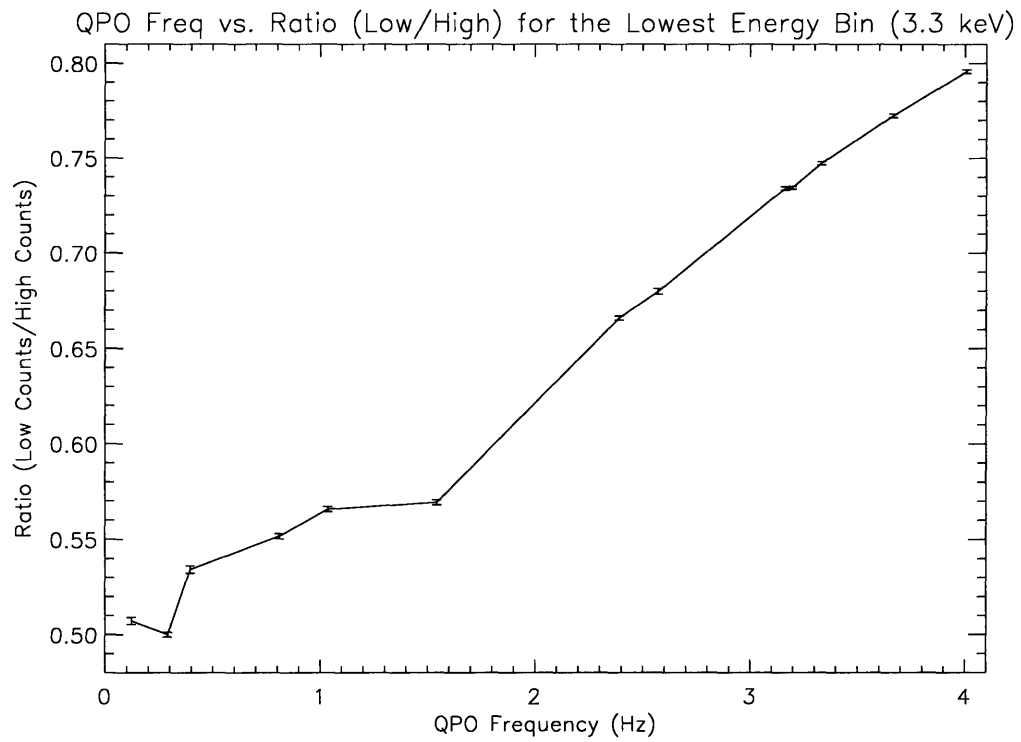
Figure 3-11: Ratio plot of *low* counts/*high* counts for the lowest energy bin, showing a nearly linear relationship between QPO frequency and ratio. However, this linear pattern is not evident in the overall rms amplitude for all energy bins (see Figure 3-3).

Chapter 4

Discussion

The goal of our research was to study the spectra of the black hole X-ray binary XTE J1550−564 as a function of *high* and *low* intensity in the phase of the QPO. Through careful selection of periods of *high* and *low* intensity phases of the QPOs, we were able to study both the temporal as well as the spectral properties of the QPOs simultaneously. The spectra in *high* and *low* intensity QPO phase were compared over a range of average source flux levels ($\sim$2-6$\times10^{-8}ergs\ cm^{-2}s^{-1}$, see Cui et al. (1999)) and QPO frequencies (0.1-4 Hz). The main result of this work is that changes in the Fe Kα line in relation to changes in QPO intensity can vary dramatically over a timescale of less than a day. At times, the flux of the Fe Kα can be correlated with changes in the intensity of the QPO. In a matter of hours, however, it can show strong anti-correlation in which the ratio of Fe Kα flux (*high/low*) can go from less than half to nearly 5 times the continuum flux ratio. As our results demonstrate, QPO behavior must be studied over many observations to determine consistent trends in behavior. Where such consistency occurs, a possible link between two independent diagnostics of the inner accretion flow may be involved.

Assuming a black hole mass of 9.61 M$_\odot$ (Orosz et al. 2002), if the QPO frequencies in our study correspond to Keplerian orbits, then the slowest QPO (0.122 Hz) and the fastest QPO (4.01 Hz) in our study correspond to radii of 454 R$_{Schw}$ and 44.4 R$_{Schw}$ respectively. These radii are much too far from the compact object to dominate the X-ray flux and cause the QPOs. Hence, we can exclude the possibility of the QPOs corresponding to Keplerian frequencies. The energy in an accretion disk must be dissipated closer to the black hole.

4.0.1 Observed Differences

We fit the spectra in observations 1 and 2 with a broken power law and a Gaussian. The results for these observations are listed in Table 3.1 and Table 3.2. The power law indices ranged from $\sim$1.35-1.62 (observation 1) and $\sim$1.47-1.69 (observation 2). In these observations, the Gaussian was centered around $\sim$6.4 keV, signifying the Fe Kα emission line. Initial results from these observations revealed that the Fe Kα line equivalent width, rather than increasing during intervals of *high* intensity, appeared to remain constant. In other words, the Fe line flux appeared to rise and fall at the same rate as the continuum flux (within measurement errors).

We were also able to fit observation 1 with the pexrav reflection model (see Magdziarz and Zdziarski 1995) and a Gaussian. The results for observation 1 are listed in Table 3.3. Again, the Gaussian was centered around $\sim$6.4 keV, and no significant difference was observed in the equivalent widths of the Gaussians (within measurement errors). The flux of

the Fe Kα line also rose and fell at the same rate as the continuum flux (within measurement errors), meaning that the relative contribution from the Fe line to the overall flux did not change. The reflection indices, on the other hand, revealed a decrease from the average in the *high* intensity spectra and a small increase from the average in the *low* intensity spectra. In other words, an increase in intensity led to a decrease in the amount of relative reflection. Within measurement errors, no significant changes in power law indices were observed. The fluxes, equivalent widths, and their ratios are given in Table 3.3. We attempted to apply the pexrav model to later observations, but we could not get a χ^2(dof) better than 2.48(47) even when applied to the average spectra.

Beginning with observation 3, however, the addition of an absorption edge ∼9 keV was necessary to improve the fit (it improved the original χ^2(dof) in observation 3 from 3.79(46) to 0.44(44)). Because the absorption edge was found at energies above the Fe Kα line (as were most of the residuals), we were still able to obtain information in the Fe line region by fitting observations 3-13 with a broken power law, a Gaussian, and an absorption edge.

In observations 1-13, we found many changes in the spectrum, as evidenced in Table 3.5. In 5 observations, no significant differences in Fe line equivalent width were detected (within measurement errors). In those same observations, the Fe line flux rose and fell at the same rate as the continuum (within measurement errors). In 6 observations, the Fe line flux exceeded the increase in continuum flux by nearly a factor of 5. This was also evident in an increase in equivalent width. Finally, in 2 observations, the Fe line flux actually fell well short (by about 50%) of the increase in continuum flux (within measurement errors). Hence, no patterns were observed in the spectra.

On the other hand, a ratio plot of *low* counts/*high* counts for the lowest energy bin revealed a nearly linear relationship between QPO frequency and ratio (and, thus, variability) (see Figure 3-11). All points on the plot fall within 7% of the best-fit line. Ratio plots of all observations together (see Figure 3-10) confirmed that the rms decreases (higher ratio) with QPO frequency. The ratios also showed that the rms increases (lower ratio) with energy up to about 10 keV, above which it decreases slightly (higher ratio). The shape of the ratio curves (ratio vs. energy) at low energies is nearly identical for the later observations (7-13). In other words, the average slope of the ratio curves below 10 keV (slope≡Δratio/Δenergy) does not change by more than 20% in these observations. By comparison, the average slope of the first 5 observations differs from the average slope of the last 7 observations by ∼90%.

Similar to Cui et al. (see Cui et al. 1999), we found a strong anti-correlation between the frequency of the QPO and its strength. The rms also decreased with QPO frequency. The ratios of the *low* intensity and *high* intensity count rates in the 3.3-31 keV energy range indicate an increase in the QPO strength (lower ratio) up to about 10 keV, above which it decreases only slightly (see Figure 3-10). The fact that the shape of the ratio curves (ratio vs. energy) at low energies is nearly identical for these observations suggests that the disk component is probably not contributing to the QPO variability. The change in QPO frequency between observations 6 and 7 (where the disk blackbody emerges) is a transition from ∼1.5 Hz to ∼2.4 Hz (see Table 2.1).

4.0.2 Model Predictions

Several spectral models attempt to explain QPO behavior based on changes in the common disk plus corona picture of the region near a black hole (see Figure 4-1). Such models attempt to explain observed differences in equivalent widths of the Fe Kα line. For example, one model arises from a purely geometric description of the inner accretion disk (e.g, Miller

50

and Homan (2005)). This geometric model contends that QPOs could be created by blobs or warps in the inner accretion disk that could give a quasi-periodically changing reflector area (see Figure 4-2). Such a change in the reflector area would give more surface area for the central X-ray source to irradiate, resulting in increased reflection as well. Fe Kα emission is part of the "reflection" process, so increased reflection would signal an increase in the strength of the Fe Kα line in the observed spectrum. Moreover, if photons passing through the hot corona/jets are upscattered to higher energies (e.g., through inverse Comptonization), this effect could also explain any observed variations in either the continuum intensity or in any emission line intensity.

Consider a blob or warp in the accretion disk located on the far side of the black hole (see Figure 4-2). Such a structure would effectively increase the amount of reflector area, thereby increasing the relative strength of the Fe Kα line compared to the continuum. In other words, the line equivalent width would increase along with the increase in observed flux. For example, an observed flux of 10 may be comprised of direct flux of 6 and reflected flux of 4. However, if the reflector area increases such that the reflected flux goes from 4 to 6, the direct flux of 6 does not change, but the observed flux becomes 12. Thus, the relative contribution from reflection goes from $4/10 = 0.4$ to $6/12 = 0.5$. The Fe Kα line always constitutes the same fraction of the reflected flux. If it constitutes $1/2$ of the reflected flux, then the relative strength of the Fe line compared to the observed flux shows an increase from $2/10 = 0.2$ to $3/10 = 0.3$, meaning that the equivalent width increases.

Basic Disk Reflection
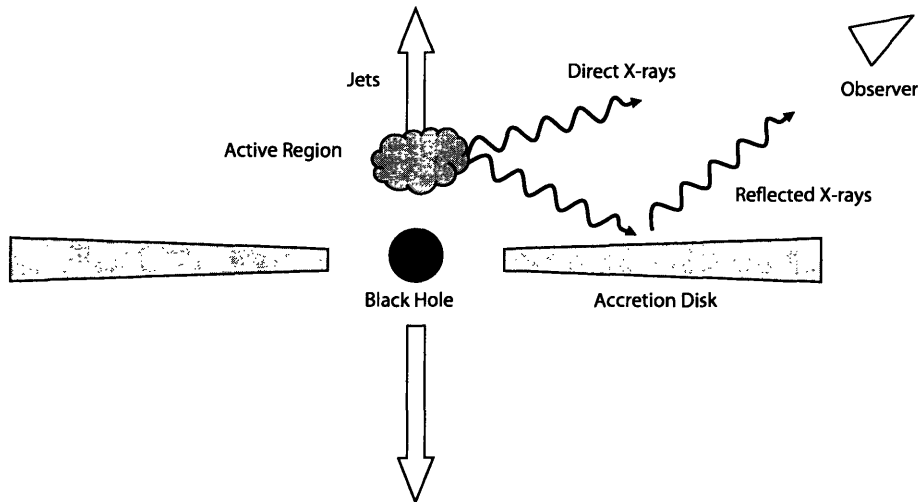
Figure 4-1: A schematic representation of the common disk plus corona picture often assumed for the region near a black hole.

Alternatively, a disk precession model (see Stella et al. 1999) argues that a precessing accretion disk is responsible for QPOs. In this model (see Figure 4-3), the accretion disk

Blob or Warp on Disk
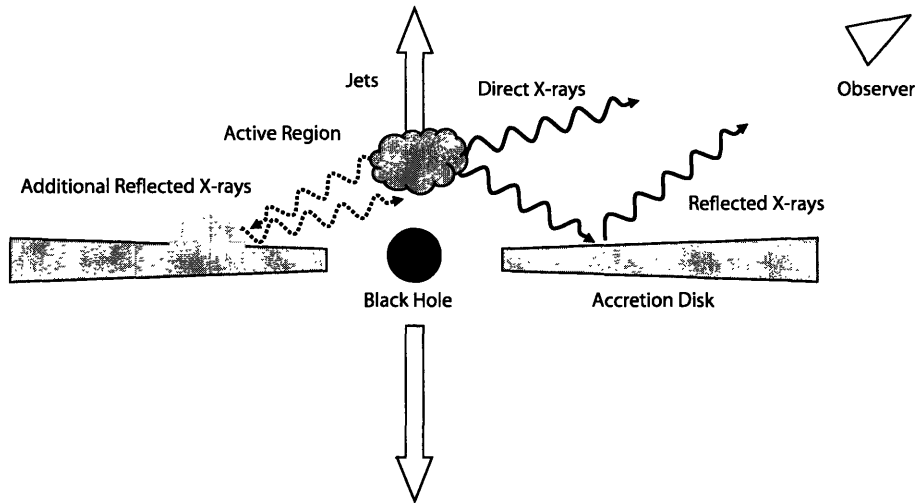
Figure 4-2: A schematic representation of a blob or warp in the inner accretion disk that could give a quasi-periodically changing reflector area. Such a change in the reflector area would give more surface area for the central X-ray source to irradiate, resulting in increased reflection (and increased line equivalent width) as well.

itself wobbles, or tilts, in its orbit around the black hole. Rather than tracing out an orbit confined to a stationary plane, the accretion disk instead traces out a plane that is constantly changing. This precession creates a repeating pattern of geometric changes in the relationship between the observer, the accretion disk, and the hot, active regions near the black hole, resulting in a quasi-periodically changing reflector area. During times of increased reflection (i.e., when the disk is tilted toward the observer as in Figure 4-3), stronger Fe Kα line emission (increased equivalent width) would be observed, as in the numerical example above.

Still other models purport that QPOs are caused by a changing corona or changing jets that are the active regions emitting hard X-rays near the compact object (see Figure 4-4). The flux from these sources would undoubtedly irradiate the inner accretion disk, which would, in turn, process or reflect the incident photons. Thus, an episodic modulation of the hard flux component could result in changes in intensity of X-rays reflected off of the accretion disk. This model, however, does not predict a change in equivalent width of the Fe Kα line. Instead, it predicts that the flux of the Fe line will rise and fall at the same rate as the flux of the continuum.

A similar model (e.g., George and Fabian (1991) or Magdziarz and Zdziarski (1995)) attributes changes in observed intensity to changes in the height of the emitting region above the disk (see Figure 4-5). For instance, as the hot corona irradiates the disk, a move toward or away from the disk would cause changes in observed intensity. When the hot

Precessing Disk
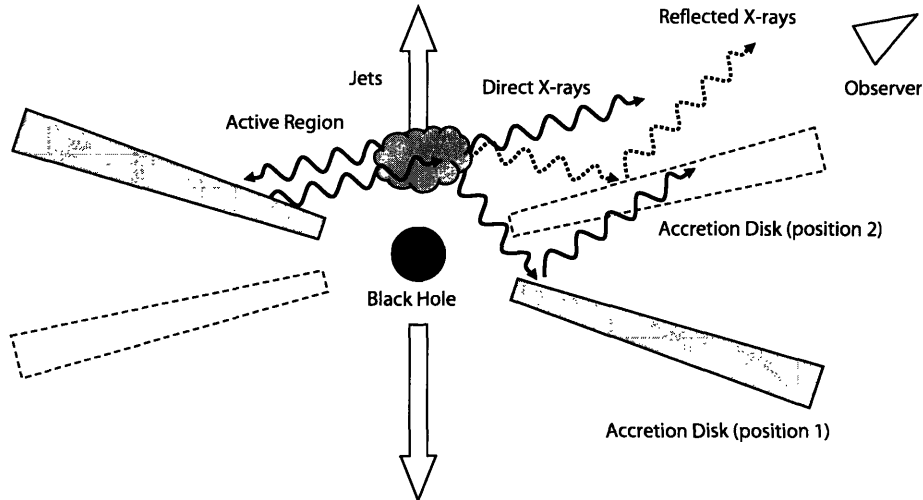
Figure 4-3: A schematic representation of a precessing disk. The accretion disk itself wobbles, or tilts, in its orbit around the black hole, resulting in a quasi-periodically changing reflector area. During times of increased reflection when the disk is tilted toward the observer (position 1), stronger Fe Kα line emission (increased equivalent width) would be observed.

Model	EW increases	No Change in EW
Disk Precession	Yes	No
Blob or Warp on Disk	Yes	No
Changing Corona Intensity	No	Yes
Changing Corona Height	Yes	No

Table 4.1: Table of four models and their predictions about what happens to the equivalent width (EW) of the Fe Kα line when observed intensity increases. "Yes" means that the model makes that prediction, and "No" means that it does not.

corona moves closer to the surface of the disk, the efficiency of reflection increases, thereby increasing the fraction of the lightcurve attributed to reflection from the disk. Conversely, a move away from the disk would have the opposite effect. Because the amount of reflected flux changes, the Fe line equivalent width also changes, as previously described.

These models make predictions about the observed spectra from X-ray binaries that exhibit QPOs. In particular, they predicate their beliefs on interpretations of the Fe Kα line. The models contend that changes in observed intensity are accompanied by specific behavior in Fe Kα line emission, as evidenced by changes in equivalent width. These models along with their predictions are listed in Table 4.1.

Changing Source Intensity
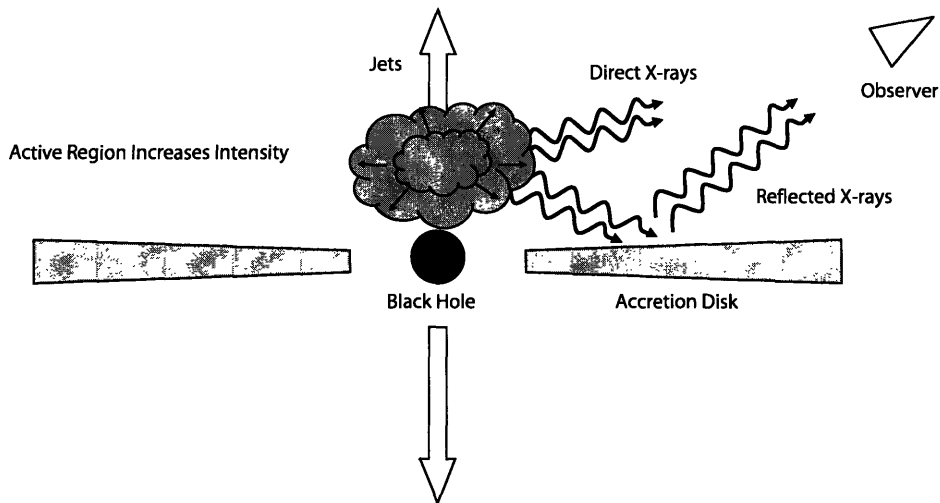
Figure 4-4: A schematic representation of a change in the active region (corona or jets). An increase in intensity of these active regions would also result in an increase in intensity of reflected radiation from the disk.

4.0.3   Comparison with Models

After we started this research, Miller and Homan (see Miller and Homan 2005) made a similar study for the black hole X-ray binary GRS 1915+105. They found a significant difference in the Fe $K\alpha$ line equivalent width between the *high* and *low* intensities in the 1-2 Hz QPO. They reported a ratio of equivalent widths (*low*/*high*) of 0.60±0.03. Based on their study of two observations, they reported new evidence in favor of a model in which QPO frequencies are associated with phenomena closer to the black hole, such as relativistic periastron precession of slightly eccentric orbits or nodal precession of slightly tilted orbits at the inner disk (e.g., Stella et al. (1999)). They suggested that a quasi-periodically changing reflector area due to Lense-Thirring precession could modulate changes in continuum flux and line flux (see Miller and Homan 2005).

After studying several observations, we found the same behavior in the data of XTE J1550−564, but it was not the *only* behavior we found. In the first 2 observations, we found a ratio of equivalent widths (*low*/*high*) of 1.07±0.10 in the fit using the broken power law and a Gaussian, and 1.10±0.11 in the fit using the pexrav reflection model and a Gaussian. This shows that, in the data of observations 1 and 2, the integrated flux of the Fe $K\alpha$ line was proportional to the flux of the continuum. In other words, the Fe $K\alpha$ line strength was correlated with the source flux in the *high* and *low* intensity of the QPO. In our study, 5 out of 13 observations behaved this way. These 5 observations of the QPOs in XTE J1550−564 do not show the same behavior as the 2 reported in GRS 1915+105. The results of these

Changing Height of Corona
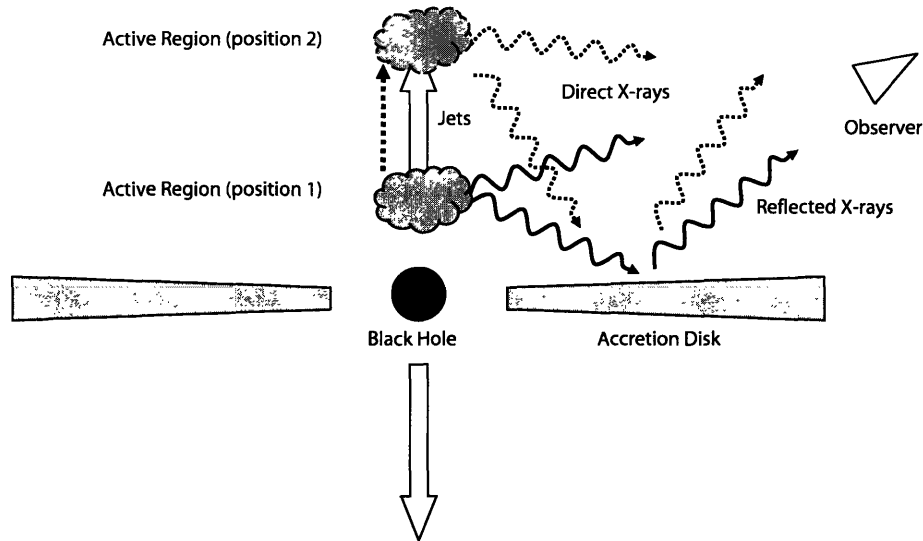
Figure 4-5: A schematic representation of a change in height of the active region above the disk. As the active region moves away from the disk, the efficiency of reflection decreases, resulting in a decrease of reflected intensity.

observations alone suggest that the QPOs are not the result of disk precession. For the same reason, they are likely not due to a structure on the disk (blob or warp) or a change in height of the active regions (corona/jets).

However, 6 out of 13 observations show the same behavior as those reported for GRS 1915+105, suggesting that the same models excluded above could indeed play a role in producing the QPOs. Judging by the ratio plot of Fe $K\alpha$ line flux versus time (Figure 3-9), we might easily have picked 2 consecutive observations whose results are consistent with those of Miller and Homan. This notion increases the importance of considering multiple observations for study. Perhaps further study of GRS 1915+105 will reveal observational results that are in opposition to the initial 2 observations. Our results show that some observations differ from the predictions made by Miller and Homan (2005), but they still support Miller and Homan's suggestion of a possible link between discrete timing features (QPOs) and spectral features (Fe $K\alpha$ emission lines) which occur in the inner disk around black holes. This evidence strengthens the notion of using the changing correlation/anti-correlation between the Fe $K\alpha$ line and QPOs to study the innermost relativistic environment around black holes.

In addition to supporting or refuting explanations for the QPO behavior in XTE J1550$-$564 in terms of geometry, our data can also address a model in which QPOs are modulated by the underlying intensity variations in the source of hard X-rays. Such a model purports that QPOs are caused by changes in the intensity of the corona or jets that are emitting hard X-rays near the compact object (see Figure 4-4). The flux from these sources irradiates the

inner accretion disk, which, in turn, reflects the incident photons. Thus, an episodic modulation of the hard flux component could result in changes in intensity of X-rays reflected off of the accretion disk. The Fe Kα emission line is part of this "reflected" radiation. In the case of a change in source intensity, the equivalent width of the Fe line would not change because the line constitutes the same fraction of the reflected radiation regardless of the source intensity. In our study, 5 out of 13 observations gave evidence in support of this model.

However, data from observation 1 suggest that this model alone cannot account for the behavior of the relative reflection indices, which is not what is expected from a mere change in hard flux intensity. Spectral fits using the pexrav reflection model (Magdziarz and Zdziarski 1995) showed that the *high* intensity phase actually has a *lower* reflection fraction than the *low* intensity phase. In other words, the reflection indices revealed a *decrease* from the average in the *high* intensity spectra and a small *increase* from the average in the *low* intensity spectra. This could be explained in terms of beaming of the hard emission (e.g., Miniutti and Fabian (2004)). The reflection fraction is given by R= $\Omega/2\pi$ =reflected/direct emission. If we over-estimate the amount of direct emission by assuming an isotropic source of hard X-ray emission when the source is actually beamed, we get a falsely low reflection fraction (see Figure 4-6). This would mean that the hard component is more beamed in the *high* intensity phase of the QPO than in the *low* intensity phase. Our findings may support a current model for light bending near to a black hole which predicts this (e.g., Miniutti and Fabian (2004)). In this model, hard photons emitted by regions at a small height above the accretion disk are bent toward the disk by the strong gravitational field of the black hole, thereby enhancing the continuum that illuminates the disk while greatly reducing the continuum of direct emission that reaches the observer. Alternatively, beaming could be due to the relativistic jets that are emitting hard photons above the disk. Since particles in the jets are moving at relativistic speeds, we do not expect them to emit isotropically, but rather mostly in their direction of travel.

Judging from the ratio plots (see Figure 3-10) and the plot of ratio vs. QPO frequency (see Figure 3-11), the decrease in rms at low energy could be due to the accretion disk component, as discussed in Chapter 1. Temperatures in a hot inner accretion disk are expected to be ∼10-20 million K. Such a hot inner disk could serve as a source of soft-seed photons (∼1-2 keV), effectively increasing the number of observed low-energy photons and, hence, increasing the ratio. The disk component would affect the low-energy ratios of each observation in the same way, which would explain how the shape of the ratio curves (ratio vs. energy) at low energies is nearly identical (within 7%) for these observations. As the disk component becomes more important in its relative contribution to the spectrum, the effect would be an increase in the ratio (decrease in rms). Although the disk component may not vary, the fraction of the spectrum constituted by the disk component might indeed vary. Applying this interpretation to the last 7 observations (7-13), we believe we might be seeing increasing contributions to the spectra from the disk blackbody component. Steadily increasing importance of the disk blackbody component could cause the dramatic change in the QPO strength (higher ratios) observed at low energies. And as Figure 3-11 shows, the relative importance of the disk component has a nearly linear correlation with increasing QPO frequency at the lowest energy.

We do not know what causes the QPOs in XTE J1550−564. In fact, the 13 observations in our study displayed 3 competing effects. In some regards, we know that the behavior of QPOs in XTE J1550−564 differs from that of the black hole X-ray binary GRS 1915+105; yet in some observations, they are alike. Our data provide evidence of complex mechanisms

Beaming of Hard Photons
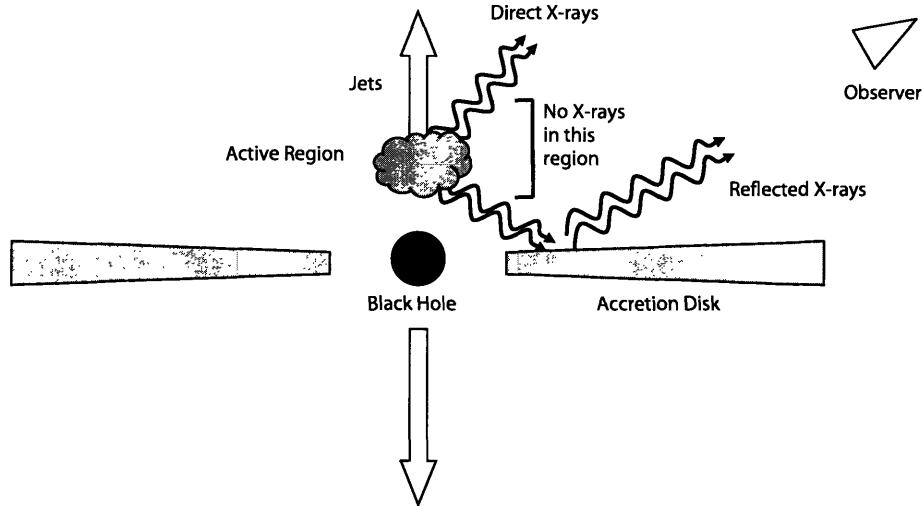
Figure 4-6: A schematic representation of beaming of the hard emission from the active region (corona or jets). Instead radiating isotropically, the active regions may radiate as beams in only limited directions. In this model, hard photons emitted by regions at a small height above the accretion disk are bent toward the disk by the strong gravitational field of the black hole, thereby enhancing the continuum that illuminates the disk while greatly reducing the continuum of direct emission that reaches the observer. Alternatively, beaming could be due to the relativistic jets that are emitting hard photons above the disk. Since particles in the jets are moving at relativistic speeds, we do not expect them to emit isotropically, but rather mostly in their direction of travel. If we over-estimate the amount of direct emission by assuming an isotropic source of hard X-ray emission when the source is actually beamed, we get a falsely low reflection fraction.

that can cause multiple effects. An accurate model should be able to explain these varying phenomena. Further exploration of these correlations and anti-correlations may be able to determine better models. Regardless of the mechanism at work, our data show that current explanations for QPOs have some physical basis, suggesting that QPOs could be due to a variety of intervening processes and circumstances from episodic modulation of the hard flux component in the corona or jets to relativistic nodal precession. In the end, the findings of our work support the basic disk plus corona picture that often has been assumed based on far weaker evidence.

Chapter 5

Conclusion

Due to its high time resolution and large collecting area, the *Rossi X-ray Timing Explorer* has played a key role in facilitating the study of QPOs and variability in X-ray sources. After analyzing 13 observations (and using two different methods of spectral fitting for one), our analysis of 0.1-4 Hz QPOs from the black hole X-ray binary XTE J1550−564 has yielded results that are indicative of complex mechanisms that go beyond any single current model.

In comparison to previous work done by Miller and Homan using observations of the black hole X-ray binary GRS 1915+105 (Miller and Homan 2005), our findings from 6 of 13 observations support the idea of an Fe Kα−QPO correlation evidenced by changes in Fe line equivalent width. In the study of 2 observations, Miller and Homan found that the equivalent width of the Fe Kα line *increased* with the *high* intensity phase of the QPO. Our results from 6 out of 13 observations supported that claim. However, our results from 5 observations showed *no change* in the equivalent width with the *high* intensity phase of the QPO, and results from 2 observations showed an actual *decrease* in equivalent width. Hence, our results suggest that the QPOs observed in XTE J1550−564 are not the result of only a single model based on disk precession, a structure on the disk (blob or warp), or a change in height of the active regions (corona/jets).

In some cases, we found that the flux of the Fe Kα line was correlated with the flux of the continuum: the line flux rose and fell at the same rate as the continuum (within measurement errors), thereby confirming a positive correlation. In other cases, we found that the flux of the Fe Kα line was anti-correlated with the flux of the continuum. Despite these differences, our results support Miller and Homan's suggestion of a link between discrete timing features (QPOs) and spectral features (Fe Kα emission lines) which occur in the inner disk around black holes. This evidence strengthens the notion of using the Fe Kα line and its correlation with QPOs to study the innermost relativistic environment around black holes. It also suggests that the correct model should be able to explain both the correlation and anti-correlation in XTE J1550−564 as well as the behavior observed in GRS 1915+105.

Rather than supporting a single explanation for the QPO behavior in XTE J1550−564 in terms of geometry, our data also support a model in which QPOs could be modulated by the underlying intensity variations in the source of hard X-rays. Such a model purports that QPOs are caused by changes in the intensity of the corona or jets that are emitting hard X-rays near the compact object (see Figure 4-4). The flux from these sources irradiates the inner accretion disk, which, in turn, reflects the incident photons. Thus, an episodic modu-

59

lation of the hard flux component could result in changes in intensity of X-rays reflected off of the accretion disk. The Fe Kα emission line is part of this "reflected" radiation. In the case of a change in source intensity, the equivalent width of the Fe line would not change because the line constitutes the same fraction of the reflected radiation regardless of the source intensity.

However, the data also suggest that this model alone cannot account for the behavior of the relative reflection indices, which is not what is expected from a mere change in hard flux intensity. Spectral fits from one observation using the pexrav reflection model (Magdziarz and Zdziarski 1995) showed that the *high* intensity phase actually has a *lower* reflection fraction than the *low* intensity phase. In other words, the reflection indices revealed a *decrease* from the average in the *high* intensity spectra and a small *increase* from the average in the *low* intensity spectra. This could be explained in terms of beaming of the hard emission (e.g., Miniutti and Fabian (2004)). The reflection fraction is given by R= $\Omega/2\pi$ =reflected/direct emission. If we over-estimate the amount of direct emission by assuming an isotropic source of hard X-ray emission when the source is actually beamed, we get a falsely low reflection fraction (see Figure 4-6). This would mean that the hard component is more beamed in the *high* intensity phase of the QPO than in the *low* intensity phase. Our findings may support a current model for light bending near to a black hole which predicts this (e.g., Miniutti and Fabian (2004)). However, it is also possible that our results are affected by the limited spectral resolution and range of the data.

Even though the origins of QPOs have not been resolved, we are continuing to advance our understanding of the properties associated with QPOs. Continued observations with *RXTE* using long exposures and carefully selected PCA modes may provide more information to further constrain the properties of QPOs. Newer satellites with large collecting areas and good energy resolution, such as *XMM-Newton* or *Astro-E2*, may support further studies as well. Through our increased understanding and insight into the mechanisms of QPOs, we will be able to more accurately explain their origins.

Bibliography

M. R. Bate. The formation of binary and multiple stars in clusters. In *Revista Mexicana de Astronomia y Astrofisica Conference Series*, pages 175–183, August 2004.

H. V. Bradt, R. E. Rothschild, and J. H. Swank. X-ray timing explorer mission. *A&AS*, 97:355–360, January 1993.

D. Campbell-Wilson, V. McIntyre, R. Hunstead, A. Green, R. B. Wilson, and C. A. Wilson. XTE J1550-564. *IAU Circ.*, 7010:3–+, September 1998.

S. Corbel, R. P. Fender, A. K. Tzioumis, J. A. Tomsick, J. A. Orosz, J. M. Miller, R. Wijnands, and P. Kaaret. Large-Scale, Decelerating, Relativistic X-ray Jets from the Microquasar XTE J1550-564. *Science*, 298:196–199, October 2002.

W. Cui, S. N. Zhang, W. Chen, and E. H. Morgan. Strong Aperiodic X-Ray Variability and Quasi-Periodic Oscillationin X-Ray Nova XTE J1550-564. *ApJ*, 512:L43–L46, February 1999.

I. M. George and A. C. Fabian. X-ray reflection from cold matter in active galactic nuclei and X-ray binaries. *MNRAS*, 249:352–367, March 1991.

D. Hannikainen, D. Campbell-Wilson, R. Hunstead, V. McIntyre, J. Lovell, J. Reynolds, T. Tzioumis, and K. Wu. XTE J1550-564: a superluminal ejection during the September 1998 outburst. *Astrophysics and Space Science Supplement*, 276:45–48, 2001.

P. Magdziarz and A. A. Zdziarski. Angle-dependent Compton reflection of X-rays and gamma-rays. *MNRAS*, 273:837–848, April 1995.

J. M. Miller and J. Homan. Evidence for a Link between Fe Kα Emission-Line Strength and Quasi-periodic Oscillation Phase in a Black Hole. *ApJ*, 618:L107–L110, January 2005.

G. Miniutti and A. C. Fabian. A light bending model for the X-ray temporal and spectral properties of accreting black holes. *MNRAS*, 349:1435–1448, April 2004.

K. Mitsuda, H. Inoue, K. Koyama, K. Makishima, M. Matsuoka, Y. Ogawara, K. Suzuki, Y. Tanaka, N. Shibazaki, and T. Hirano. Energy spectra of low-mass binary X-ray sources observed from TENMA. *PASJ*, 36:741–759, 1984.

J. Orosz, C. Bailyn, and R. Jain. XTE J1550-564. *IAU Circ.*, 7009:1–+, September 1998.

J. A. Orosz, P. J. Groot, M. van der Klis, J. E. McClintock, M. R. Garcia, P. Zhao, R. K. Jain, C. D. Bailyn, and R. A. Remillard. Dynamical Evidence for a Black Hole in the Microquasar XTE J1550-564. *ApJ*, 568:845–861, April 2002.

R. A. Remillard, G. J. Sobczak, M. P. Muno, and J. E. McClintock. Characterizing the Quasi-periodic Oscillation Behavior of the X-Ray Nova XTE J1550-564. *ApJ*, 564:962–973, January 2002.

G. J. Sobczak, J. E. McClintock, R. A. Remillard, W. Cui, A. M. Levine, E. H. Morgan, J. A. Orosz, and C. D. Bailyn. Complete RXTE Spectral Observations of the Black Hole X-ray Nova XTE J1550-564. *ApJ*, 544:993–1015, December 2000.

L. Stella, M. Vietri, and S. M. Morsink. Correlations in the Quasi-periodic Oscillation Frequencies of Low-Mass X-Ray Binaries and the Relativistic Precession Model. *ApJ*, 524:L63–L66, October 1999.

R. E. Taam and B. A. Fryxell. The hydrodynamics of accretion from stellar winds. *American Scientist*, 77:539–545, December 1989.

M. van der Klis. *in X-ray binaries.* Cambridge Astrophysics Series, Cambridge, MA: Cambridge University Press, —c1995, edited by Lewin, Walter H.G.; Van Paradijs, Jan; Van den Heuvel, Edward P.J., 1995. Chapter 6, p. 252.

J. van Paradijs and J. E. McClintock. *in X-ray binaries.* Cambridge Astrophysics Series, Cambridge, MA: Cambridge University Press, —c1995, edited by Lewin, Walter H.G.; Van Paradijs, Jan; Van den Heuvel, Edward P.J., 1995. Chapter 2, p. 58.

N. E. White, F. Nagase, and A. N. Parmar. *in X-ray binaries.* Cambridge Astrophysics Series, Cambridge, MA: Cambridge University Press, —c1995, edited by Lewin, Walter H.G.; Van Paradijs, Jan; Van den Heuvel, Edward P.J., 1995. Chapter 1, p. 1.

A. A. Zdziarski and M. Gierliński. Radiative Processes, Spectral States and Variability of Black-Hole Binaries. *Progress of Theoretical Physics Supplement*, 155:99–119, 2004.

Appendix A

IDL codes

build_histo

```
pro build_histo,time,rate,filtered,a,b,c,d,e,g
;
; This program takes the original times and rates from b.lc,
; filters the lightcurve with a band-pass filter, finds local extrema,
; ensures that there are equal numbers of maxima and minima to form pairs,
; and then outputs the differences in count rate between each maximum-
; minimum pair for the purpose of building a histogram.
;
; The program starts by reading in the time and rate from b.lc.
;
print, 'Reading Time Column'
ftab_ ext, 'b.lc', 'time', time, exten_no=1
print, 'Reading Rate Column'
ftab_ext, 'b.lc', 'rate', rate, exten_no=1
print, 'Reading Error Column'
ftab_ext, 'b.lc', 'error', error, exten_no=1
;
; The following code can be used to generate power-density spectra.
;
; fourier=fft(rate(0:8191))
; power=abs(fourier(1:4096))^2
; print, power
; freq=(findgen(4096)+1.0)/4096
; newfreq=rebin(freq,256)
; newpower=rebin(power,256)
;
; The program next creates a band-pass digital filter.
; The first two paramenters are the low-freq and high-freq that
; define the band-pass in terms of the Nyquist freq.
; The output is the filtered lightcurve.
;
filter=digital_filter(.1229,.1239,50,5)
```

```
binsize=0.15625
filtered=convol(rate,filter)
;
; The program next identifies local maxima.
;
n1=n_elements(filtered)
a=dblarr(2,n1)
a[0,*]=time
a[1,*]=filtered
b=dblarr(2,n1)
b[0,0]=-1
b[1,0]=-1
b[0,n1-2]=-1
b[1,n1-2]=-1
for i=11,n1-2 do begin
if a[1,i] gt a[1,i-1] and a[1,i] gt a[1,i+1] then begin
b[0,i]=a[0,i]
b[1,i]=a[1,i]
endif else begin
b[0,i]=-1
b[1,i]=-1
endelse
endfor
;
; The program next reduces the array to only the data points
; corresponding to the maxima.
;
b[0,n1-1]=-1
b[1,n1-1]=-1
c=dblarr(2,n1)
ccount=01
for bcount=01,n1*2-1 do begin
if b(bcount) ne -1 then begin
c(ccount)=b(bcount)
ccount=ccount+1
endif
endfor
n=min(where(c[1,*] eq 0))
c=c[*,0:n-1]
;
; The program then identifies local minima.
;
n2=n_elements(c)/2
d=dblarr(2,n1)
d[0,0]=-1
d[1,0]=-1
d[0,n1-2]=-1
d[1,n1-2]=-1
```

64

```
for i=11,n1-2 do begin
if a[1,i] lt a[1,i-1] and a[1,i] lt a[1,i+1] then begin
d[0,i]=a[0,i]
d[1,i]=a[1,i]
endif else begin
d[0,i]=-1
d[1,i]=-1
endelse
endfor
;
; The program then reduces the array to only the data points
; corresponding to the minima.
;
d[0,n1-1]=-1
d[1,n1-1]=-1
e=dblarr(2,n1)
ecount=0l
for dcount=0l,n1*2-1 do begin
if d(dcount) ne -1 then begin
e(ecount)=d(dcount)
ecount=ecount+1
endif
endfor
p=min(where(e[1,*] eq 0))
e=e[*,0:p-1]
;
; The program next ensures that the number of local maxima
; is equal to the number of minima in order to form pairs.
;
n3=n_elements(e)/2
f=c[*,0:n3-1]
;
; The program then determines the difference in count rate
; between the maximum and minimum in each pair.  All of the
; resulting arrays are sent to IDL, where they are used to
; build a histogram of the differences in count rate.
; The largest and smallest difference are printed and recorded.
; The overall max and min of the original lightcurve are also printed
; for recording purposes.
;
g=f[1,*]-e[1,*]
print,max(rate)
print,min(rate)
print,mean(rate)
print,max(g)
print,min(g)
print,mean(g)
end
```

find_extrema

```
pro find_extrema,time,rate,filtered,a,b,c,d,e,highs,highs_keep,lows,lows_keep,
times_h,times_l,times_high,times_low
;
; This program takes the original times and rates from b.lc,
; filters the lightcurve with a band-pass filter, finds local extrema,
; excludes maximum-minimum pairs whose difference in count rate falls below 75%
; of the mode difference, excludes maximum-minimum pairs that occur in time
; closer than 6 times the binsize, and then outputs the resulting
; times_high.txt and times_low.txt.  ;
; The program starts by reading in the time and rate from b.lc.
;
print, 'Reading Time Column'
ftab_ext, 'b.lc', 'time', time, exten_no=1
print, 'Reading Rate Column'
ftab_ext, 'b.lc', 'rate', rate, exten_no=1
print, 'Reading Error Column'
ftab_ext, 'b.lc', 'error', error, exten_no=1
; ; The program next creates a band-pass digital filter.
; The first two paramenters are the low-freq and high-freq that
; define the band-pass in terms of the Nyquist freq.
; The output is the filtered lightcurve.
; filter=digital_filter(.1229,.1239,50,5)
binsize=0.15625
filtered=convol(rate,filter)
;
; The program next identifies local maxima.
;
n1=n_elements(filtered)
a=dblarr(2,n1)
a[0,*]=time
a[1,*]=filtered
b=dblarr(2,n1)
b[0,0]=-1
b[1,0]=-1
for i=11,n1-2 do begin
if a[1,i] gt a[1,i-1] and a[1,i] gt a[1,i+1] then begin
b[0,i]=a[0,i]
b[1,i]=a[1,i]
endif else begin
b[0,i]=-1
b[1,i]=-1
endelse
endfor
```

```
b[0,n1-1]=-1
b[1,n1-1]=-1
;
; The program then identifies local minima.
;
d=dblarr(2,n1)
d[0,0]=-1
d[1,0]=-1
for i=1l,n1-2 do begin
if a[1,i] lt a[1,i-1] and a[1,i] lt a[1,i+1] then begin
d[0,i]=a[0,i]
d[1,i]=a[1,i]
endif else begin
d[0,i]=-1
d[1,i]=-1
endelse
endfor
d[0,n1-1]=-1
d[1,n1-1]=-1
;
; The program then reduces the arrays to only the data points
; corresponding to the selected maxima and minima.
;
for i=2,20 do begin
good=where(b ne -1)
good1=where(d ne -1)
goodb=b(good)
goodd=d(good1)
if n_elements(goodb) gt n_elements(goodd) then begin
b[0,n1-i]=-1
b[1,n1-i]=-1
endif
endfor
;
;
c=dblarr(2,n1)
ccount=0l
for bcount=0l,n1*2-1 do begin
if b(bcount) ne -1 then begin
c(ccount)=b(bcount)
ccount=ccount+1
endif
endfor
n=min(where(c[1,*] eq 0))
c=c[*,0:n-1]
;
;
e=dblarr(2,n1)
```

```
ecount=01
for dcount=01,n1*2-1 do begin
if d(dcount) ne -1 then begin
e(ecount)=d(dcount)
ecount=ecount+1
endif
endfor
p=min(where(e[1,*] eq 0))
e=e[*,0:p-1]
;
; The program next excludes maximum-minimum pairs whose difference in count
; rate falls below 75% of the mode difference.  It then reduces the arrays
; to only the data points corresponding to the selected maxima and minima.
; n2=n_elements(c)/2
highs=dblarr(2,n2)
lows=dblarr(2,n2)
for i=01,n2-1 do begin
if c[1,i]-e[1,i] gt 4.5 then begin
highs[0,i]=c[0,i]
highs[1,i]=c[1,i]
lows[0,i]=e[0,i]
lows[1,i]=e[1,i]
endif else begin
highs[0,i]=-1
highs[1,i]=-1
lows[0,i]=-1
lows[1,i]=-1
endelse
endfor
highs_keep=dblarr(2,n2)
highs_keepcount=01
for highscount=01,n2*2-1 do begin
if highs(highscount) ne -1 then begin
highs_keep(highs_keepcount)=highs(highscount)
highs_keepcount=highs_keepcount+1
endif
endfor
z=min(where(highs_keep[1,*] eq 0))
highs_keep=highs_keep[*,0:z-1]
lows_keep=dblarr(2,n2)
lows_keepcount=01
for lowscount=01,n2*2-1 do begin
if lows(lowscount) ne -1 then begin
lows_keep(lows_keepcount)=lows(lowscount)
lows_keepcount=lows_keepcount+1
endif
endfor
z=min(where(lows_keep[1,*] eq 0))
```

```
lows_keep=lows_keep[*,0:z-1]
;
; The program next excludes maximum-minimum pairs that occur in time
; closer than 6 times the binsize.
;
n3=n_elements(highs_keep)/2
for i=1,n3-1 do begin
if highs_keep[0,i]-highs_keep[0,i-1] lt 6*binsize then begin
highs_keep[0,i]=-1
highs_keep[1,i]=-1
endif
if lows_keep[0,i]-lows_keep[0,i-1] lt 6*binsize then begin
lows_keep[0,i]=-1
lows_keep[1,i]=-1
endif
endfor
;
; The program then outputs the resulting times_high.txt and times_low.txt.
;
times_h=dblarr(n3*3)
times_l=dblarr(n3*3)
for i=0,n3-1 do begin
times_h[3*i+1]=highs_keep[0,i]
times_h[3*i]=highs_keep[0,i]-binsize
times_h[3*i+2]=highs_keep[0,i]+binsize
times_l[3*i+1]=lows_keep[0,i]
times_l[3*i]=lows_keep[0,i]-binsize
times_l[3*i+2]=lows_keep[0,i]+binsize
endfor
;
;
;
times_high=dblarr(2,n3*3)
times_low=dblarr(2,n3*3)
times_high[0,*]=times_h
times_high[1,*]=times_h+binsize
times_low[0,*]=times_l
times_low[1,*]=times_l+binsize
;
;
;
openw,1,'times_high.txt'
printf,1,times_high,format='(e24.14,e24.14)'
close,1
openw,1,'times_low.txt'
printf,1,times_low,format='(e24.14,e24.14)'
close,1
end
```

time_list_high

```
pro time_list_high,a,b,n1
;
; This program inputs times_high.txt and consolidates each group of
; consecutive time intervals into one long interval for use in saextrct
; and seextrct.
;
openr,1,'times_high.txt'
a=dblarr(2,2334)
readf,1,a
close,1
n1=n_elements(a)/2
for i=0,n1-2 do begin
if a[1,i] eq a[0,i+1] then begin
a[1,i]=-1
a[0,i+1]=-1
endif
endfor
b=dblarr(2,n1)
bcount=0
for acount=0,n1*2-1 do begin
if a(acount) ne -1 then begin
b(bcount)=a(acount)
bcount=bcount+1
endif
endfor
n=min(where(b[1,*] eq 0))
b=b[*,0:n-1]
openw,1,'times_high_new.txt'
printf,1,b,format='(e24.14,e24.14)'
close,1
end
```

time_list_low

```
pro time_list_low,a,b,n1
;
; This program inputs times_low.txt and consolidates each group of
; consecutive time intervals into one long interval for use in saextrct
; and seextrct.
;
openr,1,'times_low.txt'
a=dblarr(2,2334)
```

```
readf,1,a
close,1
n1=n_elements(a)/2
for i=0,n1-2 do begin
if a[1,i] eq a[0,i+1] then begin
a[1,i]=-1
a[0,i+1]=-1
endif
endfor
b=dblarr(2,n1)
bcount=0
for acount=0,n1*2-1 do begin
if a(acount) ne -1 then begin
b(bcount)=a(acount)
bcount=bcount+1
endif
endfor
n=min(where(b[1,*] eq 0))
b=b[*,0:n-1]
openw,1,'times_low_new.txt'
printf,1,b,format='(e24.14,e24.14)'
close,1
end
```

make_ratio

```
pro make_ratio,av_energies,ratios,errors
;
; This program makes a ratio plot of low counts/high counts with error bars.
;
; The program starts by reading in the average energy for each bin as well as
; the high count rate and low count rate for each bin.
;
openr,1,'av_energies2'
av_energies=dblarr(19)
readf,1,av_energies
close,1
openr,1,'highcnts.txt'
highs1=dblarr(2,19)
readf,1,highs1
close,1
openr,1,'lowcnts.txt'
lows1=dblarr(2,19)
readf,1,lows1
close,1
;
```

```
; The program then multiplies each count rate by the appropriate exposure time
; to obtain the number of counts.
;
bh_exp=342.9805
evh_exp=342.9805
bl_exp=342.9805
evl_exp=342.9805
highs=highs1[1,*]
highs[0:6]=highs[0:6]*bh_exp
highs[7:18]=highs[7:18]*evh_exp
lows=lows1[1,*]
lows[0:6]=lows[0:6]*bl_exp
lows[7:18]=lows[7:18]*evl_exp
;
; The program next calculates the ratios and the errors, and then plots both.
;
ratios=lows/highs
errors=ratios*sqrt((sqrt(lows)/lows)$^2$+(sqrt(highs)/highs)$^2$)
openw,1,'highcnts.txt'
printf,1,highs
close,1
openw,1,'lowcnts.txt'
printf,1,lows
close,1
openw,1,'ratios.txt'
printf,1,ratios
close,1
openw,1,'errors.txt'
printf,1,errors
close,1
set_plot,'ps'
device,filename='ratioplot.ps'
plot,av_energies,ratios,/xlog,xrange=[3,40],/xstyle,yrange=[.35,.65],/ystyle,
title='30188-06-01-01 Ratio of Low Counts/High Counts',xtitle='Channel Energy
(keV)',
ytitle='Ratio (Low/High)'
errplot,av_energies,ratios-errors,ratios+errors
device,/close
set_plot,'x'
end
```